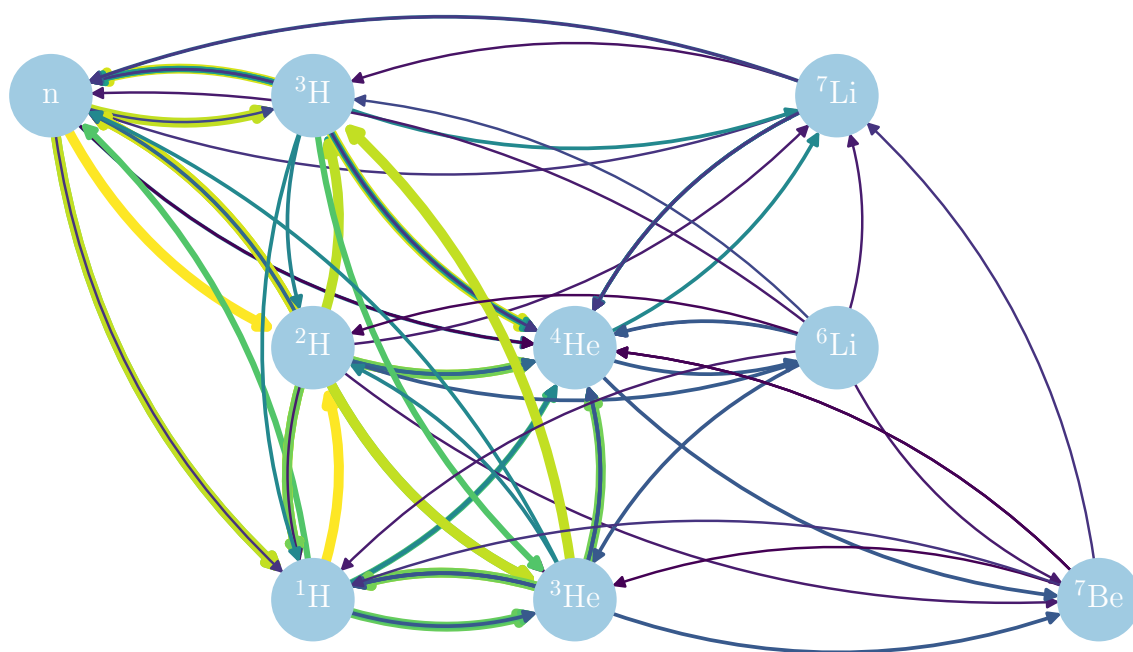


APODORA: A NOVEL CODE FOR DESCRIBING BIG BANG NUCLEOSYNTHESIS

APODORA:
EN NY KODE TIL AT BESKRIVE BIG BANG KERNESYNTESSE



HANS BRÜNER DEIN
201706079

MASTER'S THESIS IN PHYSICS
FEBRUARY 2024

SUPERVISORS: THOMAS TRAM & STEEN HANNESTED

DEPARTMENT OF PHYSICS AND ASTRONOMY
AARHUS UNIVERSITY

Colophon

APODORA: A Novel Code for Describing Big Bang Nucleosynthesis

— *APODORA: En ny kode til at beskrive Big Bang Kernesyntese*

Master's thesis by Hans Brüner Dein. Written under supervision by Asc.Prof. Thomas Tram & Prof. Steen Hannested Department of Physics and Astronomy, Aarhus University.

Typeset by the author with L^AT_EX and the memoir document class, using Linux Libertine and Linux Biolinum 11.0/13.6pt.

Printed at Aarhus University

Abstract (English)

The goal of this thesis is to present the development of a new BBN code APODORA (Adaptable Python interface Offering Determination Of Relic Abundances). APODORA is designed to be more flexible than existing codes, with an emphasis on the use of modern standardized computing methods. Derivations of the equations describing the time evolution of various components in the early universe are presented. These are implemented in a flexible IPython environment with the reaction network being created using interfaces from pynucastro[31]. The numerical uncertainty associated with every relevant input parameter of the code is systematically examined to ensure a high level of numerical precision. An in-depth comparison between APODORA and ALTERBBN is performed, demonstrating equal or superior precision and speed. Finally, the resulting final abundances from APODORA are compared with multiple existing BBN codes as well as observational data.

Resumé (Dansk)

Målet med dette speciale er at præsentere udviklingen af en ny BBN-kode APODORA, (Adaptable Python interface Offering Determination Of Relic Abundances). APODORA er skabt med henblik på at være mere fleksible end eksisterende løsninger, men særlig fokus på anvendelsen af moderne og standardiserende løsningsmetoder. Udlædning af ligningerne som beskriver tidsudviklingen af det tidlige univers bestanddele bliver præsenteret. Dette er implementeret i et fleksibelt IPython miljø, hvortil reaktionsnetværket bliver skabt ved hjælp af brugerflader fra pakken pynucastro[31]. Den numeriske usikkerhed forbundet med hver relevant inputparameter i koden undersøges systematisk, for at sikre et højt niveau af numerisk præcision. Der udføres en dybdegående sammenligning af APODORA og ALTERBBN, som viser at både hastighed og præcision er lige så god, hvis ikke bedre. Til sidst sammenlignes forudsigelserne fra APODORA med andre BBN-koder samt observationer.

Acknowledgements

First and foremost, I would like to thank my friends and family for their invaluable support throughout my time at IFA. For this thesis, I would like to thank my supervisor, Thomas Tram, and unofficial co-supervisor, Steen Hannested, for helping me along the way and ensuring I reached the goal in the end. I would also like to thank Erik Steenberg, Camilla Sørensen, Emil Birk, and Marta Jensen for proofreading the first and second drafts of this thesis. In addition, I want to thank all the people in the cosmology group, and 1520-823, particularly Christiane Rahbek, for providing company during the long days and nights of writing this thesis. I would also like to thank the pynucastro team for being very helpful in quickly fixing bugs and adding necessary features, with special thanks to Michael Zingale. Finally, I would like to thank my grandfather for igniting the passion for science, which led me to pursue physics.

Contents

Introduction	v
Objective	vi
Outline	vi
1 BBN Physics and Cosmology	1
1.1 Determining Background Parameters	1
1.1.1 Scale Factor	1
1.1.2 Temperature	2
1.1.3 Additional Parameters	2
1.2 Energy Density and Pressure of Different Particles	2
1.2.1 Relativistic Gasses	3
1.2.2 Photons	4
1.2.3 Neutrinos	4
1.2.4 Electrons and Positrons	5
1.2.5 Baryons	7
1.3 Nuclear Reactions	9
1.3.1 Proton to neutron rate	9
1.4 Initial Conditions	10
1.4.1 Initial Temperature	10
1.4.2 Initial Time	10
1.4.3 Initial Time in Existing Literature	12
1.4.4 Initial Abundances	13
2 BBN code	15
2.1 A Brief History of BBN Codes	15
2.1.1 Modern Codes	15
2.1.2 APODORA	16
2.2 Integrating the System of Equations	16
2.2.1 Integration Methods	16
2.2.2 Initial Conditions	17
2.2.3 Simplifications of the Problem	17
2.3 Creating the Reaction Network	18
2.4 Running APODORA	20
3 Results and Discussion	21
3.1 Accuracy	24
3.1.1 Tolerances	24

3.1.2	Electron Energy	24
3.1.3	Interpolation	27
3.1.4	Network Timings	27
3.1.5	Neutrino Decoupling	30
3.2	Comparison with ALTERBBN	31
3.2.1	Speed	31
3.2.2	Predicted Abundances	32
3.2.3	Background	32
3.2.4	Reaction Network	34
3.2.5	Modifying the Network with AlterBBN rates	35
3.3	Final Abundances	36
3.3.1	Eta and the Lithium Problem	38
3.4	Outlook	40
4	Conclusion	41
	Bibliography	43
A	Plots of Reaction rates during BBN	47

Introduction

Everything we see around us is made of atoms, which at their core contain a nucleus. Atomic nuclei are the fundamental building blocks that make up the stars, planets, and the humans that live on them. Understanding the creation of atomic nuclei is to understand the origin of the world itself.

A Brief History of Early Nucleosynthesis

When the universe was only a microsecond old, quarks coalesced to form the first protons and neutrons[32]. Initially, there was an equal amount of neutrons and protons, but as the universe cooled, the slightly lighter protons became favored. The neutrons and protons remained in thermal equilibrium until the universe cooled to around 10^{10} K, a second after the Big Bang. Here, the interaction between neutrinos and baryons becomes too weak to maintain thermodynamic equilibrium, freezing the ratio of neutrons and protons at one to five. The protons and neutrons can fuse to create deuterium, but these nuclei are short-lived as their low binding energy makes them vulnerable to destruction by the abundant high-energy photons. As these photons cool, the average lifetime of deuterium increases, giving the deuterium nuclei more time to combine into much more stable helium nuclei. The rate of helium creation increases until it becomes great enough to rapidly convert all available neutrons into helium at approximately 200 seconds. Due to the delay caused by deuterium, the temperature and density of the universe will be too low to create any more than trace amounts of heavier elements. And so, a few minutes after it began, primordial nucleosynthesis ends. Barring radioactive decay, the abundance of the various elements will remain unchanged until the first stars appear 10^8 years later[30]. The first computer code describing this process was created by Robert Wagoner in the late sixties[4]. Since then, many others have followed, with each implementation having its advantages and disadvantages.

Objective

The objective of this thesis is to create a new state-of-the-art BBN code from first principles. To differentiate this code from existing implementations, it must fulfill these five requirements:

- **Accessibility:** The code needs to run on any machine without the use of any proprietary software or special environments.
- **Accuracy:** The results must be consistent with those of contemporary BBN codes. Additionally, the results must be internally consistent with well-constrained numerical errors.
- **Alacrity:** The code must be as fast as other contemporary BBN codes.
- **Agnostic reaction rates:** The code should use nuclear reaction rates from a single publicly available database to avoid any bias in rate selection.
- **Adaptability:** The code should be flexible and allow the investigation of various physical processes without changing the basic structure.

Outline

This thesis has three main parts:

First, we will go over the physics required to describe the Big Bang nucleosynthesis. This will entail deriving every necessary relation from fundamental equations of cosmology, statistical physics, and thermodynamics.

Next, we will review the numerical implementation of BBN. We start by covering the history and numerical difficulties associated with BBN calculations. The implementation of APODORA will then be briefly discussed, including the steps taken to overcome the aforementioned numerical difficulties.

Finally, we will look at the results. First, we will look at how APODORA can be used to get an overview of the various nuclear processes during BBN. Then, we will discuss the numerical accuracy of the code and how different parameters influence the precision. Ultimately, we compare with the results of other codes and observations.

Terminology

In the later sections of the thesis, predicted values for various nuclear abundances will be shown. For historical reasons, these are usually given as a molar fraction relative to the abundance of hydrogen. That is to say, the number of nucleons contained in the particular isotope relative to the amount of free protons. ${}^4\text{He}$ is an exception and is instead expressed as a fraction of total nucleons and denoted by Y_p . Though not entirely accurate, both of these molar fractions are often referred to as mass fractions.

As BBN represents a crossover of nuclear physics and astronomy, temperature is interchangeably measured in MeV and Kelvin. Here, it is helpful to remember $\text{MeV} = 11.6 \times 10^9 \text{K}$ or simply $\text{MeV} \approx 10^{10} \text{K}$.

BBN Physics and Cosmology

To understand the process of Big Bang nucleosynthesis, we must examine the intersection between cosmology, thermodynamics, particle, nuclear and statistical physics. Though this might seem daunting, it turns out that the unique conditions during this epoch allow for extensive simplifications of this otherwise monumental task. Throughout this thesis, we use $\hbar = c = k_B = 1$.

1.1 Determining Background Parameters

Nuclear processes in the early universe are governed by two main parameters, the density of the baryons and their temperature. The density will decrease as the universe expands, so we need to track this expansion using the scale factor a , which is a simple dimensionless scalar proportional to the expansion of the universe. In the early universe, baryons were in thermodynamic equilibrium with the photons, so to track their temperature, we just need to track the temperature of the photons, T .

1.1.1 Scale Factor

BBN takes place after inflation while the universe is still radiation-dominated. The expansion can be described by the Friedman equation, which can be simplified with the reasonable approximation that both curvature and the cosmological constant are zero [11, (4.29)].

$$H^2 = \left(\frac{\dot{a}}{a}\right)^2 = \frac{8\pi G}{3}\rho_{tot}, \quad (1.1)$$

with H being the Hubble parameter, G the gravitational constant, and ρ_{tot} referring to the total energy density of photons, leptons, and baryons,

$$\rho_{tot} = \rho_\gamma + \rho_\nu + (\rho_{e^-} + \rho_{e^+}) + \rho_b. \quad (1.2)$$

(1.1) can be rearranged as a differential equation explicitly describing the time evolution of the scale factor.

$$\frac{da}{dt} = a \sqrt{\frac{8\pi G}{3}\rho_{tot}(T, a)} \quad (1.3)$$

1.1.2 Temperature

To find an expression for the temperature evolution, we utilize energy conservation. We can consider the neutrinos as decoupled from the other particles during BBN, and so the photon temperature will be determined by the remaining components. Since the universe at this point is very much homogeneous and isotropic, we utilize the fluid equation for adiabatic expansion [11, (4.44)] to describe the time evolution of the density of coupled components.

$$\dot{\rho}_{set} + 3\frac{\dot{a}}{a}(\rho_{set} + P_{set}) = 0 \quad (1.4)$$

With ρ_{set} being the density of none-decoupled components and P_{set} being their pressures.

$$\rho_{set} = \rho_\gamma + (\rho_{e^-} + \rho_{e^+}) + \rho_b \quad , \quad P_{set} = P_\gamma + (P_{e^-} + P_{e^+}) + P_b \quad (1.5)$$

Using the chain rule $\dot{\rho} = \dot{T}d\rho/dT$, we can then set up a differential equation describing the time evolution of the photon temperature.

$$\frac{dT}{dt} = -3\frac{\dot{a}}{a} \frac{\rho_{set}(T, a) + P_{set}(T, a)}{\frac{d\rho_{set}(T, a)}{dT}} \quad (1.6)$$

1.1.3 Additional Parameters

For this code, the only necessary cosmological parameters are the scale factor and temperature, but other BBN codes often track different parameters. Most BBN codes are based on the original code by Wagoner described in section 2.1. These don't track the scale factor but instead use the quantity h .

$$h = M_u \frac{n_b}{T_9^3}, \quad (1.7)$$

with M_u being atomic mass units, n_b the baryon number density, and T_9 the temperature in 10^9 Kelvin. This quantity was useful since it stays approximately constant throughout BBN while being easy to directly convert to baryon density. However, with modern computers, this numerical simplicity is inconsequential, and as such, it is more instructive to track the scale factor. The electron chemical potential was also tracked by the Wagoner code and its successors. The main effect of this is ensuring a non-zero electron density after $e^- e^+$ annihilation. We can easily set this to 0, as the impact will be 3 orders of magnitude lower than the already minuscule impact of the baryon density.

1.2 Energy Density and Pressure of Different Particles

To solve eqs. (1.3) and (1.6), we need to know the density and pressure of the components of the early universe. To do this, we first need to derive the general equations for the energy and pressure of a collection of relativistic particles before going over each component.

1.2.1 Relativistic Gasses

In the very early universe, most particles were in thermal equilibrium and can thus be described by the rules of statistical physics. Here, the average number of particles in a given state is governed by the Fermi-Dirac distribution for fermions and the Bose-Einstein distribution for bosons.

$$\bar{n}_{FD} = \frac{1}{e^{(E-\mu)/T} + 1}, \quad \bar{n}_{BE} = \frac{1}{e^{(E-\mu)/T} - 1}, \quad (1.8)$$

with E being the total energy of each particle in the state and μ the chemical potential. Using the average number of particles in a given state, the total number density can be found by integrating over all possible momentum states.

$$n(T) = \frac{g}{(2\pi)^3} \int_0^\infty \bar{n}(p, T) dp^3 = \frac{g}{2\pi^2} \int_0^\infty \bar{n}(p, T) p^2 dp, \quad (1.9)$$

with g being the degeneracy parameter, describing the number of distinct states with a given momentum. We can similarly find an expression for the energy density by multiplying the integrand by the relativistic energy $E^2 = m^2 + p^2$.

$$\rho(T) = \frac{g}{2\pi^2} \int_0^\infty \bar{n}(p, T) \sqrt{m^2 + p^2} p^2 dp \quad (1.10)$$

The pressure can be similarly determined by identifying the pressure exerted by a single relativistic particle with some momentum p . Pressure is defined as the force exerted per unit area. Consider a relativistic particle confined to a sphere of radius r . Whenever it collides with the surface, it will exert a force proportional to the change in momentum.

$$F = \frac{dp}{dt} = \frac{\Delta p}{\Delta t}, \quad \Delta p = 2p \cos \theta, \quad (1.11)$$

with θ being the incident angle.

The time between collisions can be deduced based on the distance traveled.

$$\Delta t = \frac{L}{v} = L \frac{\sqrt{m^2 + p^2}}{p}, \quad (1.12)$$

with distance between collisions L , and velocity v . Where we have used $p = mv$ and $E = \gamma m$ to relate velocity to momentum.

Next, consider the triangle created by the center of the sphere and two consecutive collision points. Using the law of cosines, we can determine L ,

$$r^2 = L^2 + r^2 + 2Lr \cos \theta \Rightarrow L = 2r \cos \theta. \quad (1.13)$$

Combining eqs. (1.11) to (1.13), we can determine the force and pressure exerted on the sphere by each particle.

$$F = \frac{p^2}{r \sqrt{m^2 + p^2}}, \quad P = \frac{p^2}{4\pi r^3 \sqrt{m^2 + p^2}} \quad (1.14)$$

Generalizing this for any volume, we get a quantity analogous to the energy of a single particle,

$$PV = \frac{p^2}{3\sqrt{m^2 + p^2}}. \quad (1.15)$$

Integrating with PV will give us the total pressure, just as integrating with energy gives the energy density.

$$P(T) = \frac{g}{6\pi^2} \int_0^\infty \bar{n}(p, T) \frac{p^4}{\sqrt{m^2 + p^2}} dp \quad (1.16)$$

Additionally, we see that the pressure of an ultra-relativistic gas follows a simple relation.

$$P(T) = \frac{\rho(T)}{3} \quad (\text{for } m \ll p) \quad (1.17)$$

With this, we can determine the density and pressure of each component, starting with the photons.

1.2.2 Photons

Photons are massless bosons with two distinct polarizations for each momentum state. With $g = 2$, we use (1.10) to determine the energy density.

$$\rho_\gamma(T) = \int_0^\infty \frac{p^3}{\pi^2} \frac{1}{e^{p/T} - 1} dp = \frac{T^4}{\pi^2} \int_0^\infty \frac{u^3}{e^u - 1} du \quad (1.18)$$

By changing the integration variable to $u = p/T$, the integral becomes a well-known representation of the Riemann Zeta function [33, (25.5.1)], with the following solution

$$\rho_\gamma(T) = \frac{T^4}{\pi^2} \Gamma(4) \zeta(4) = \frac{\pi^2}{15} T^4. \quad (1.19)$$

From this, we can easily determine the temperature derivative and pressure.

$$\frac{d\rho_\gamma(T)}{dT} = \frac{4}{15} \pi^2 T^3, \quad P_\gamma(T) = \frac{\rho_\gamma(T)}{3} \quad (1.20)$$

The same procedure can be used to determine the number density,

$$n_\gamma(T) = \frac{T^3}{\pi^2} \int_0^\infty \frac{u^2}{e^u - 1} du = \frac{T^3}{\pi^2} \Gamma(3) \zeta(3). \quad (1.21)$$

1.2.3 Neutrinos

For neutrinos $g = 2N_\nu$, to account for the different species and their antiparticles.

$$\rho_\nu(T_\nu) = N_\nu \int_0^\infty \frac{p^3}{\pi^2} \frac{1}{e^{p/T_\nu} + 1} dp = N_\nu \frac{T_\nu^4}{\pi^2} \int_0^\infty \frac{u^3}{e^u + 1} du \quad (1.22)$$

This is another integral representation of the Riemann Zeta function [33, (25.5.3)].

$$\rho_\nu(T_\nu) = N_\nu \frac{T_\nu^4}{\pi^2} \Gamma(4) \zeta(4) (1 - 2^3) = N_\nu \frac{7}{8} \frac{\pi^2}{15} T_\nu^4. \quad (1.23)$$

This relation only holds if the neutrinos follow a Fermi-Dirac distribution, which is not exactly true at later times since their gradual decoupling from the other components introduces non-thermal distortions to their energy distribution. However, if the neutrinos are completely decoupled, their energy can instead be described using only the scale factor

$$\rho_\nu(t) = \frac{\rho_\nu(T_i)}{a(t)^4}, \quad (1.24)$$

with T_i being the initial temperature where neutrinos are still in thermal equilibrium and $a = 1$. This has the added advantage of eliminating the need to track neutrino temperature. The major downside is that this does not account for the small energy transfer from $e^+ e^-$ -annihilation due to incomplete decoupling of neutrinos. To compensate, we can replace the number of neutrinos $N_\nu = 3$ with an effective neutrino number $N_\nu^{\text{eff}} = 3.045$, (Salas and Pastor [18]), corresponding to the predicted increase in energy. The impact of incomplete neutrino decoupling is discussed further in section 3.1.5.

1.2.4 Electrons and Positrons

Since electrons and positrons have mass, solving for their density and pressure is a lot more intricate than for the massless particles.

$$\rho_\pm(T) = \frac{1}{\pi^2} \int_0^\infty \frac{\sqrt{m^2 + p^2}}{e^{(E \pm \mu)/T} + 1} p^2 dp \quad (1.25)$$

$$P_\pm(T) = \frac{1}{3\pi^2} \int_0^\infty \frac{1}{e^{(E \pm \mu)/T} + 1} \frac{p^4}{\sqrt{m^2 + p^2}} dp \quad (1.26)$$

Inspired by the derivation of Chandrasekhar [1], we will solve these integrals by using the rapidity θ .

$$\sinh \theta = \frac{p}{m}, \quad \cosh \theta = \frac{E}{m} \quad (1.27)$$

After a simple change of variable, we get a much nicer form of the integrals.

$$\rho_\pm(T) = \frac{m^4}{\pi^2} \int_0^\infty \frac{\sinh^2 \theta \cosh^2 \theta}{e^{(m \cosh \theta \pm \mu)/T} + 1} d\theta \quad (1.28)$$

$$P_\pm(T) = \frac{m^4}{3\pi^2} \int_0^\infty \frac{\sinh^4 \theta}{e^{(m \cosh \theta \pm \mu)/T} + 1} d\theta \quad (1.29)$$

Next, we start by considering the geometric series.

$$\frac{1}{1+x} = \sum_{n=0}^{\infty} (-1)^n x^n, \quad \text{for } |x| < 1 \quad (1.30)$$

Multiplying both sides by x grants us a very useful expansion,

$$\frac{1}{x^{-1} + 1} = \sum_{n=1}^{\infty} (-1)^{n+1} x^n \quad , \quad \text{for } |x| < 1. \quad (1.31)$$

Before and during BBN, $(E \pm \mu)/T$ will be strictly positive, enabling $x = e^{-(E \pm \mu)/T}$.

$$\frac{1}{e^{(m \cosh \theta \pm \mu)/T} + 1} = \sum_{n=1}^{n=\infty} (-1)^{n+1} e^{-n \frac{m}{T} \cosh \theta} e^{\mp n \frac{\mu}{T}} \quad (1.32)$$

The chemical potential does not depend on the rapidity, allowing us to get the combined pressure of both electrons and positrons, using $e^{-\phi} + e^{\phi} = 2 \cosh \phi$

$$P_e(T) = P_- + P_+ = \frac{2m^4}{3\pi^2} \sum_{n=1}^{n=\infty} (-1)^{n+1} \cosh \left(n \frac{\mu}{T} \right) \int_0^{\infty} e^{-n \frac{m}{T} \cosh \theta} \sinh^4 \theta d\theta \quad (1.33)$$

These terms are integral representations of modified Bessel functions [33, (10.32.8)].

$$\int_0^{\infty} e^{-z \cosh \theta} \sinh^4 \theta d\theta = 4 \frac{\Gamma(2 + \frac{1}{2})}{\sqrt{\pi} z^2} K_2(z) = 3z^{-2} K_2(z) \quad (1.34)$$

With $z = n \frac{m}{T}$, we can get the total pressure expressed as a sum of modified Bessel functions.

$$P_e(T) = \frac{2m^2}{\pi^2} T^2 \sum_{n=1}^{n=\infty} \frac{(-1)^{n+1}}{n^2} \cosh \left(n \frac{\mu}{T} \right) K_2 \left(n \frac{m}{T} \right) \quad (1.35)$$

The energy density can be found in the same way by first utilizing the identity $\cosh^2 = \sinh^2 + 1$ to get the energy density in terms of $\sinh \theta$.

$$\rho_e(T) = \rho_- + \rho_+ = \frac{2m^4}{\pi^2} \sum_{n=1}^{n=\infty} (-1)^{n+1} \cosh \left(n \frac{\mu}{T} \right) \int_0^{\infty} e^{-n \frac{m}{T} \cosh \theta} (\sinh^4 \theta + \sinh^2 \theta) d\theta \quad (1.36)$$

The \sinh^4 term is clearly the same as for the pressure up to a factor of 3. Comparing this to the results for massless particles, this term can be interpreted as the thermal energy of the electron gas. The second term also corresponds to a modified Bessel function, though of first rather than second-order [33, (10.32.8)]. Combined, this grants us the sum describing the total energy density of electrons and positrons.

$$\rho_e(T) = \frac{2m^2}{\pi^2} T^2 \sum_{n=1}^{n=\infty} \frac{(-1)^{n+1}}{n^2} \cosh \left(n \frac{\mu}{T} \right) \left(3K_2 \left(n \frac{m}{T} \right) + n \frac{m}{T} K_1 \left(n \frac{m}{T} \right) \right) \quad (1.37)$$

Using recursion relations for the modified Bessel functions [33, (10.29.1)], we see that this is equivalent to the expression used in other BBN codes [7].

$$3K_2(z) + zK_1(z) = 3 \frac{z}{4} [K_3(z) - K_1(z)] + zK_1(z) = \frac{z}{4} [3K_3(z) + K_1(z)] \quad (1.38)$$

$$\rho_e(T) = \frac{m^3}{2\pi^2} T \sum_{n=1}^{n=\infty} \frac{(-1)^{n+1}}{n} \cosh \left(n \frac{\mu}{T} \right) \left(3K_3 \left(n \frac{m}{T} \right) + K_1 \left(n \frac{m}{T} \right) \right) \quad (1.39)$$

As mentioned, many older BBN codes track the parameter $\phi_e = \frac{\mu}{T}$, but this is unnecessary, as the electron density after $e^- e^+$ annihilation is three orders of magnitude lower than the already negligible contribution of the baryons. So, for the remaining calculation, we set $\mu = 0$.

Finding the temperature derivative of the electron energy density can also be achieved using the recursion relations for Bessel functions [33, (10.29.2)].

$$\frac{d}{dz} \frac{1}{z} [3K_3(z) + K_1(z)] = -3[z^{-2}K_3(z) + z^{-1}K_2(z) + 3z^{-2}K_3(z)] - z^{-1}K_2 \quad (1.40)$$

$$= -12z^{-2}K_3(z) - 4z^{-1}K_2(z) \quad (1.41)$$

$$= -\frac{1}{z} [2K_4(z) - 2K_2(z) + 4K_2(z)] \quad (1.42)$$

$$= -\frac{2}{z} [K_4(z) + K_2(z)] \quad (1.43)$$

With this, we can determine the temperature derivative.

$$\frac{d\rho_e(T)}{dz} = -\frac{m^3}{\pi^2} T \sum_{n=1}^{\infty} \frac{(-1)^{n+1}}{n} \left(K_4\left(n\frac{m}{T}\right) + K_2\left(n\frac{m}{T}\right) \right) \quad (1.44)$$

$$\frac{d\rho_e(T)}{dT} = \frac{m^4}{\pi^2} \frac{1}{T} \sum_{n=1}^{\infty} (-1)^{n+1} \left(K_4\left(n\frac{m}{T}\right) + K_2\left(n\frac{m}{T}\right) \right) \quad (1.45)$$

1.2.5 Baryons

The temperatures at which BBN takes place are too low for baryon pair production. Therefore, the number density of baryons can be solely determined by the scale factor and some known density.

$$n_b(a) = \frac{a_0^3}{a^3} n_b(a_0), \quad (1.46)$$

with a_0 being the scale factor at a time when we know the corresponding number density $n_b(a_0)$. To determine baryon density $n_b(a_0)$, we use the baryon photon/ratio η , and the photon number density given by eq. (1.21),

$$n_b = n_\gamma(T)\eta \quad , \quad n_\gamma(T) = \frac{T^3}{\pi^2} \Gamma(3)\zeta(3). \quad (1.47)$$

From the CMB, we can measure the value of η during recombination, but unlike baryons, the number of photons does not remain unchanged from the start of BBN until recombination. The only significant source of photons is the annihilation of the electron-positron pairs. We can account for this using conservation of entropy. For a given species we define the entropy density [8, (3.91)],

$$s = \frac{\rho + P}{T}. \quad (1.48)$$

Setting $a = 1$ at the start of our BBN calculations, we get a relation between the total entropy before and after annihilation.

$$s_\gamma(T_{CMB})a_{CMB}^3 = s_e(T_i) + s_\gamma(T_i) \quad (1.49)$$

The photon number density is directly proportional to entropy density, both scaling with T^3 . This allows us to restate (1.49) only in terms of the initial entropy density.

$$n_Y(T_{CMB})a_{CMB}^3 = \frac{n_Y(T_i)}{s_Y(T_i)} (s_e(T_i) + s_Y(T_i)) \quad (1.50)$$

From this, we get the baryon density as a function of the initial photon and electron density and pressure.

$$n_b(a_{CMB})a_{CMB}^3 = n_Y(T_i) \left(\frac{s_e(T_i) + s_Y(T_i)}{s_Y(T_i)} \right) \eta \quad (1.51)$$

$$n_b(a) = \frac{1}{a^3} n_Y(T_i) \left(1 + \frac{\rho_e(T_i) + P_e(T_i)}{\rho_Y(T_i) + P_Y(T_i)} \right) \eta \quad (1.52)$$

with T_i being the initial temperature. Finally, to get the energy density we simply need to sum over all different nuclei.

$$\rho_b(a) = n_b(a) \sum_i Y_i m_i \quad (1.53)$$

For each isotope, m_i is the mass, and the abundance, Y_i , is the ratio between the number of nuclei and the total number of nucleons. Y_i is often defined as $Y_i = X_i/A_i$, with X_i being the mass fraction, and A_i the atomic weight [5]. The difference in per nucleon mass of different isotopes causes these two definitions to have a relative difference of 10^{-5} , which can be safely neglected when looking at total mass. Furthermore, we can approximate that all baryons have the same mass as a lone proton, which reduces (1.53) to $\rho_b(a) \approx n_b(a)m_p$.

Employing the chain rule, we can write the temperature derivative as

$$\frac{d\rho_b(a)}{dT} = -3\rho_b(a) \frac{1}{a} \frac{da}{dT}. \quad (1.54)$$

Since the universe is radiation-dominated, we can relate the scale factor and temperature as $a \propto T^{-1}$. This is not precise enough to be used for the background as a whole, especially during $e^- e^+$ -annihilation, but it will suffice for this already minor term, allowing us to evaluate the derivative

$$\frac{d\rho_b(a)}{dT} = 3\rho_b(a)T^{-1}. \quad (1.55)$$

The baryon pressure can be found using the ideal gas law.

$$P_b(a) = n_b(a)T \sum_i Y_i \quad (1.56)$$

Unlike that of the relativistic particles, the baryon pressure is several orders of magnitude lower than the density. Since the baryon density is already comparatively low, the pressure will be completely negligible.

1.3 Nuclear Reactions

All relevant nuclear reactions involve at most six different nuclei. Generally, we can write these reactions as

$$N_i X_i + N_j X_j + N_k X_k \rightleftharpoons N_n X_n + N_m X_m + N_l X_l, \quad (1.57)$$

where N_i is the number of nuclei X_i , that enter the reaction. The change in abundance Y_i of any nuclei is given by the sum of all reactions that create or destroy it.¹

$$\frac{dY_i}{dt} = \sum_{\lambda_i} \frac{N_i}{n_b} \left(\lambda_{nml \rightarrow ijk} \frac{Y_n^{N_n} Y_m^{N_m} Y_l^{N_l}}{N_n! N_m! N_l!} n_b^{(N_n+N_m+N_l)} - \lambda_{ijk \rightarrow nml} \frac{Y_i^{N_i} Y_j^{N_j} Y_k^{N_k}}{N_i! N_j! N_k!} n_b^{(N_i+N_j+N_k)} \right) \quad (1.58)$$

With λ being the reaction rate, and n_b being the baryon number density. The reaction rate $\lambda(T)$ only depends on the kinetic energy of the baryons and by extension, the photon temperature. $n_b(a)$ only depends on the scale factor as shown in (1.52).

From (1.58), we can quite easily determine the partial derivatives required for the construction of a Jacobian.

$$\frac{\partial}{\partial Y_j} \frac{dY_i}{dt} = - \sum_{\lambda_{ijk \rightarrow}} N_i N_j \lambda_{ijk \rightarrow nml} \frac{Y_i^{N_i} Y_j^{N_j-1} Y_k^{N_k}}{N_i! N_j! N_k!} n_b^{(N_i+N_j+N_k-1)} \quad (1.59)$$

$$\frac{\partial}{\partial Y_n} \frac{dY_i}{dt} = \sum_{\lambda_{n \rightarrow i}} N_i N_n \lambda_{nml \rightarrow ijk} \frac{Y_n^{N_n-1} Y_m^{N_m} Y_l^{N_l}}{N_n! N_m! N_l!} n_b^{(N_n+N_m+N_l-1)} \quad (1.60)$$

1.3.1 Proton \rightleftharpoons Neutron Rate

At $T > 10^{10}\text{K}$, any created nuclei will be instantly destroyed by high-energy photons. This leaves only the conversion between neutrons and positrons, which is governed by the following reactions

$$n \leftrightarrow p + e^- + \bar{\nu}_e \quad (1.61)$$

$$n + e^+ \leftrightarrow p + \bar{\nu}_e \quad (1.62)$$

$$n + \nu_e \leftrightarrow p + e^- \quad (1.63)$$

The final reaction $p \leftrightarrow n + e^+ + \nu_e$ is not possible, as it would violate energy conservation, which is apparent if one considers the reaction from the rest frame of the proton. For most other rates, we can measure λ experimentally for the forward rate $Q > 0$, and use detailed balance to estimate the corresponding reverse rate. The conditions required for maintaining nuclear statistical equilibrium between neutrons and protons cannot be achieved experimentally, and the rate must therefore be determined theoretically. This involves evaluating several integrals, which depend on both electron and neutrino density, in addition to the temperature and scale factor. Several corrections must also be made to account for the radiative, zero-temperature corrections, finite nucleon mass corrections, finite temperature radiative corrections,

1: https://pynucastro.github.io/pynucastro/rate_types.html

weak-magnetism, and QED plasma effects[21]. The final result mainly depends on temperature and experimentally determined mean neutron lifetime, τ_n . Since it isn't affected by the later reactions, it is sensible to just fit the result as a function of temperature and mean lifetime. For the default network in APODORA, the rate is described by the parameterization given in appendix C of Serpico et al. [13].

$$\lambda_{n \rightarrow p} = \frac{1}{\tau_n} e^{-q_{np}/z} \sum_{i=0}^{13} a_i z^{-i} \quad , \quad 0.01 \leq T/\text{MeV} \leq 10 \quad (1.64)$$

$$\lambda_{p \rightarrow n} = \begin{cases} \frac{1}{\tau_n} e^{-q_{pn}/z} \sum_{i=0}^{10} b_i z^{-i} & , \quad 0.1 \leq T/\text{MeV} \leq 10 \\ 0 & , \quad 0.01 \leq T/\text{MeV} \leq 0.1 \end{cases} \quad (1.65)$$

with the fitted parameters being the constants a_i and b_i as well as q_{np} and q_{pn} .

1.4 Initial Conditions

To solve this system of differential equations, we must find the initial conditions for time, the background parameters a and T , as well as the abundances Y_i . The initial value of the scale factor can be set as $a = 1$. The temperature and time are directly linked, and as none of the earlier equations have any explicit time dependence, it is more useful to choose an initial temperature and then determine the initial time based on this. Finally, the initial abundances can be determined using these conditions and nuclear statistical equilibrium (NSE).

1.4.1 Initial Temperature

When performing BBN calculations, it is most sensible to choose an initial temperature, and from it, determine all other initial conditions. The chosen temperature should be sufficiently high so that all particles are in thermal equilibrium. Most BBN codes use $T = 27 \times 10^9 \text{K}$ as the initial temperature. Higher temperatures could be used, but this is unnecessary and will often lead to numerical instabilities, which will be covered in chapter 2 and section 3.1.

1.4.2 Initial Time

Though none of the equations describing BBN have any explicit time dependence, it is still nice to know the age of the universe when it takes place. This can be achieved by integrating equation (1.6), with $T = \infty$ at $t = 0$.

$$\int_0^{t_i} dt = \int_\infty^{T_i} \left(\frac{dT}{dt} \right)^{-1} dT = - \int_\infty^{T_i} (24\pi G \rho_{\text{tot}})^{-1/2} \frac{\frac{d\rho_{\text{set}}(T)}{dT}}{\rho_{\text{set}}(T) + P_{\text{set}}(T)} dT \quad (1.66)$$

For high temperatures, we can assume that the electrons are completely relativistic. Based on the result for neutrinos (1.23), we know that the energy of a massless fermion differs from that of a boson by a factor of $7/8$. Accounting for the g factors, we get $\rho_e = 7/4 \rho_\gamma$. At temperatures above 2 MeV, the relativistic approximation deviates by less than 1%; see figure 1.1.

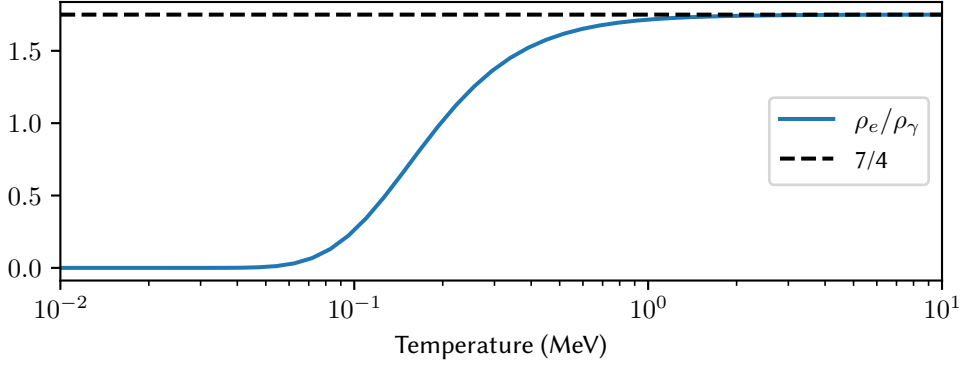


FIGURE 1.1: Exact ratio of the electron-positron energy to the photon energy.

At these temperatures, we can safely ignore the baryon contribution, which, combined with (1.17), allows us to calculate the non-decoupled terms.

$$\frac{\frac{d\rho_{set}(T)}{dT}}{\rho_{set}(T) + P_{set}(T)} = \frac{3}{4} \frac{1}{\rho_{set}(T)} \frac{d\rho_{set}(T)}{dT} = 3T^{-1} \quad (1.67)$$

For the total energy, we simply add the contributions of all components, excluding baryons,

$$\rho_{tot} = \rho_\gamma + (2 + 3) \frac{7}{8} \rho_\gamma = \frac{43}{8} \rho_\gamma \quad (1.68)$$

Inserting into (1.66), we get the initial time,

$$t_i = 3(24\pi G \frac{43}{8} \frac{\pi^2}{15})^{-1/2} \int_{\infty}^{T_i} T^{-3} dT \quad (1.69)$$

$$t_i = \frac{3}{2} (\frac{43}{5} G \pi^3)^{-1/2} T_i^{-2} \quad (1.70)$$

This relation is valid at all times before decoupling and remains approximately true at later times, as shown in figure 1.2.

To get a sense of scale for this result, we can rewrite it in units of $10^9 K$ and seconds.

$$T_9 = (43 \frac{4}{3} \pi \frac{a_r}{c^2} G)^{-1/4} t^{-1/2} = 9.97 t^{-1/2}, \quad (1.71)$$

with a_r being the radiation constant, related to the Stefan–Boltzmann constant by $a = \frac{4}{c} \sigma$. Using this, we can justify the omission of particles heavier than electrons. The lightest of these are the muon and pion, which both have masses above 100 MeV. Significant pair creation will occur at $T_9 \geq 10^3$, corresponding to $t \approx 10^4$. As such, they will have no significant impact on the initial time.

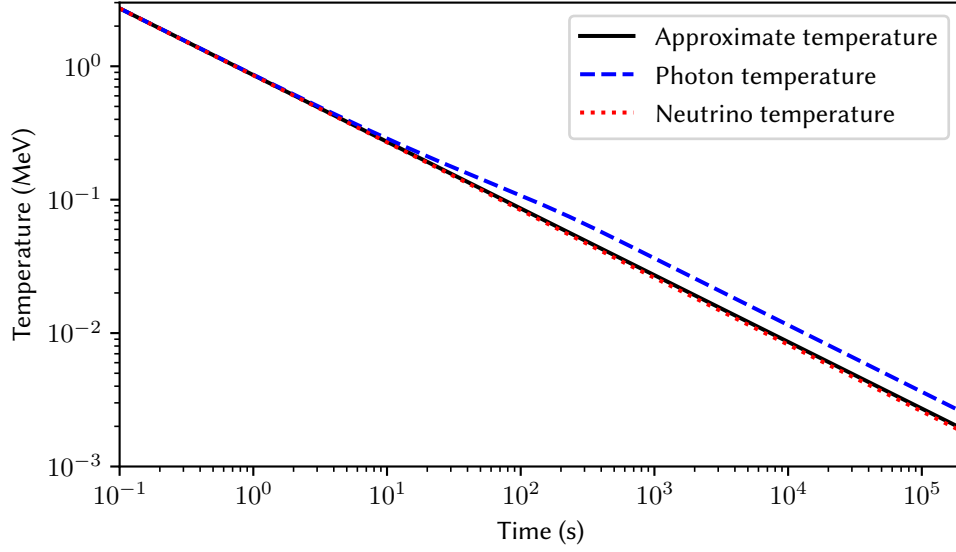


FIGURE 1.2: The temperature of photons and neutrinos during the time period of BBN, as well as the approximate temperature given by (1.70).

1.4.3 Initial Time in Existing Literature

We note that (1.71) differs significantly from the expression derived by Wagoner[4],

$$T_9 = (12\pi \frac{a_r}{c^2} G)^{1/4} t^{-1/2} = 10.4 t^{-1/2}, \quad (1.72)$$

The analytical expression is wrong, but the numerical result is correct. A simple error that probably was the result of a small mistake when transcribing the notes used for the paper. Unfortunately, this expression has been reproduced in several later BBN codes such as NUC123[7] and ALTERBBN [23]. Though Kawano reproduced the equation in the documentation, in the actual NUC123 code, he used the numerical result, and as such, the code itself had no errors. In ALTERBBN, they used natural units and so couldn't use the numerical value, leading to the error affecting the code. Additionally, they also confused the Stefan–Boltzmann and radiation constants, leading to an additional error. Examining the code, one can see that their value is wrong by 14 orders of magnitude. Since it doesn't impact final abundances, this error was only very recently discovered, with the first correction being released in 2021 by Sharpe [28],

$$T_9 = (48\pi \frac{a_r}{c^2} G)^{-1/4} t^{-1/2} = 10.4 t^{-1/2}, \quad (1.73)$$

However, this still differs from (1.71). This is due to the fact that the original derivation was performed by Wagoner in 1967, a decade before the discovery of the tau and corresponding neutrino. Though later projects correctly added the additional neutrino flavor when calculating the neutrino energy, the impact it has on the initial time had been overlooked before this thesis.

1.4.4 Initial Abundances

At the initial temperature, the only nuclei with significant abundance are the protons and neutrons, with the closest contender, deuterium, having an abundance of $Y_D \approx 10^{-12}$, fig. 3.1. Therefore, we can assume the initial abundance of all nuclei besides free neutrons and protons is zero. To find the initial abundance of neutrons and protons, we first consider the number density of protons as given by eq. (1.9),

$$n_p(T) = \frac{1}{\pi^2} \int_0^\infty \frac{1}{e^{(E-\mu_p)/T} + 1} p^2 dp. \quad (1.74)$$

As previously mentioned, the number density of baryons is minimal compared to other particles, implying that $(E - \mu)/T$ must be very large,

$$n_p(T) = \frac{1}{\pi^2} \int_0^\infty e^{(\mu_p - E)/T} p^2 dp. \quad (1.75)$$

Since protons are largely non-relativistic, we can approximate their energy by the classical expression $E = m + p^2/(2m)$,

$$n_p(T) = \frac{1}{\pi^2} e^{(\mu_p - m_p)/T} \int_0^\infty e^{-\frac{p^2}{2m_p T}} p^2 dp. \quad (1.76)$$

This is a Gaussian integral, which has a simple solution[20],

$$n_p(T) = \frac{1}{\pi^2} e^{(\mu_p - m_p)/T} \sqrt{\frac{\pi}{2}} (m_p T)^{3/2}. \quad (1.77)$$

Since all of this also applies to the neutron, we get an analogous expression

$$n_n(T) = \frac{1}{\pi^2} e^{(\mu_n - m_n)/T} \sqrt{\frac{\pi}{2}} (m_n T)^{3/2}. \quad (1.78)$$

Neutrons and protons maintain equilibrium via the reactions described in eqs. (1.61) to (1.63), allowing us to relate their chemical potential,

$$\mu_n + \mu_\nu = \mu_p + \mu_e. \quad (1.79)$$

Since the chemical potential of leptons, μ_ν and μ_e , are comparatively low[8], we can assume $\mu_n = \mu_p$. By then combining eqs. (1.77) and (1.78) we can get an expression for the neutron-to-proton ratio,

$$\frac{n_n}{n_p} = e^{(m_p - m_n)/T} \left(\frac{m_n}{m_p} \right)^{3/2}. \quad (1.80)$$

As the total number of nucleons is the sum of neutrons and protons, and almost all of them are free, we can use the definition of Y to get the following relations,

$$Y_n = \frac{n_n}{n_n + n_p} = \frac{1}{1 + \frac{n_p}{n_n}}, \quad Y_p = \frac{n_p}{n_n + n_p} = \frac{1}{1 + \frac{n_n}{n_p}}. \quad (1.81)$$

Combining eqs. (1.80) and (1.81) we get expressions for the abundances of neutrons and protons,

$$Y_n = \frac{1}{1 + e^{(m_n - m_p)/T} \left(\frac{m_p}{m_n} \right)^{3/2}}, \quad Y_p = \frac{1}{1 + e^{(m_p - m_n)/T} \left(\frac{m_n}{m_p} \right)^{3/2}}. \quad (1.82)$$

BBN code

2.1 A Brief History of BBN Codes

The concept of Big Bang nucleosynthesis is almost as old as the Big Bang Theory itself, with the idea first being proposed in the 1948 paper by Alpher, Bethe, and Gamow [2]. This early model used neutron capture and subsequent beta decay as the mechanism for BBN, though its most significant problem was the inability to explain the unusually high abundance of oxygen and carbon in the present universe. And so, it was largely supplanted by the new theory of stellar nucleosynthesis as the primary explanation for the origin of the elements.

During the following decades, it became clear that stars could not be the only explanation for the present element abundances, and with the discovery of the CMB in 1965, new attention was brought to the early universe. Only a year later, Peebles showed how simple BBN physics could be used to explain the high helium abundance unaccounted for by stellar nucleosynthesis [3].

In the following years, Wagoner created and refined the first proper BBN code, which was described in a series of defining papers[4][5][6]. The legacy of this code still heavily influences the way BBN calculations are performed today.

By the late 80s, the Wagoner code was severely outdated, with multiple inefficiencies due to, among other things, the fact that it was originally designed to run on punch cards. This inspired Lawrence Kawano to create the now ubiquitous NUC123, colloquially known as the Kawano code[7], which set the gold standard for all future BBN codes.

2.1.1 Modern Codes

In the current day and age, there exists multiple publicly available BBN codes and a countless number of private codes. The most well-known of these are PARTHENoPE, ALTERBBN, and PRIMAT.

PARTHENOPE[29] is a spiritual successor to NUC123, and like the works of Wagoner and Kawano PARTHENOPE uses FORTRAN. It retains the same structure and can generally be seen as a continually updated version of these earlier works, with features such as updated reaction rates and a user-friendly GUI.

PRIMAT[21] is a Mathematica code and unlike PARTHENOPE and ALTERBBN, it isn't directly based on the older BBN codes. The main focus of PRIMAT is improving the precision of BBN codes, specifically the ${}^4\text{He}$ abundance, which is mainly determined by the $p \rightleftharpoons n$ rates.

AlterBBN[23] is written in C and based on Kawano's NUC123. It maintains the same basic structure and integration method, though it uses natural units for everything but the reaction network, with energy defined by $\text{GeV}=1$. What separates ALTERBBN from other codes is that, as the name implies, it allows the use of alternate cosmological models and parameters. Therefore, this code is especially well suited for testing the effects these alterations have on final abundances.

2.1.2 APODORA

To fulfill the goal of **accessibility** stated in the introduction, I have chosen to use Python, as it can run on any system and currently is the most popular programming language¹. To fulfill the goal of **adaptability**, the core of APODORA will be in the form of an IPython Notebook[14]. This provides a flexible interface, allowing the code to be rapidly repurposed, which makes tests and graphics, such as those in section 3.1, much easier to produce. The most obvious issue with this is the increase in runtime since Python is not exactly known for its speed. We can, however, mitigate this using the methods presented in the following sections.

2.2 Integrating the System of Equations

The objective of any BBN code is to solve the system of differential equations described in Chapter 1, which presents some numerical difficulties.

Most nuclear reactions have a linear or quadratic dependence on density, as well as an often exponential temperature dependence. At high temperatures, this is balanced by the corresponding reverse rate being equally high. The forward and reverse rates will only cancel at the precise abundance required by nuclear statistical equilibrium (NSE). Any slight deviation from NSE, δY , will cause one rate to be slightly larger, which, due to its magnitude, will cause a huge increase in the derivative Y' .

Most numerical methods for solving differential equations are explicit and, in their simplest form, calculate the next step by adding $\Delta Y = \Delta t \cdot Y'$. If $\Delta Y > 2\delta Y$, the system will become unstable as each step will increase the absolute deviation of the next. To avoid this instability, an explicit method will have to use a minuscule step size Δt , which in practice makes the problem unsolvable.

This and similar problems are called stiff since they are very inflexible when faced with slight deviations from the "true" solution.

2.2.1 Integration Methods

Wagoner and the later codes based on this work handle the stiffness by first linearizing the system, which allows integration in an implicit form:

$$\tilde{Y}_{n+1} = (1 + C\Delta t)\tilde{Y}_n \approx (1 - C\Delta t)^{-1}\tilde{Y}_n. \quad (2.1)$$

1: <https://pypl.github.io/PYPL.html>

This is then followed by a traditional second-order Runge-Kutta integration, with ALTERBBN having options for more advanced Runge-Kutta methods.

PRIMAT on the other hand, uses a first-order BDF scheme for $T > 1.25e9$ K, switching to second-order at lower temperatures for faster computation.

I have chosen to use an implicit Runge-Kutta method of the Radau IIA family of order 5 as implemented in SciPy[25]. This method is perfectly suited to handle stiff problems such as the reaction network, and based on testing it is the most stable method among those available in SciPy.

2.2.2 Initial Conditions

As mentioned in section 1.4.4, the initial abundances of heavy nuclei are minuscule and can be set to 0 without affecting the final result. However, doing this creates large transients as the new nuclei rapidly readjust from 0 to the actual abundance required by NSE. Dealing with these transients is very time-consuming for the solver and frequently leads to crashes. To avoid this, we can set the initial abundances by requiring that the resulting right-hand-side (RHS) is 0. This minimizes the size of initial transients, making the solution faster and more stable.

2.2.3 Simplifications of the Problem

Following the example of Wagoner, most BBN codes solve the background variables and abundances concurrently. This is necessary, as they account for the change in baryon energy density and electron chemical potential caused by nucleosynthesis. Accounting for the baryon energy only results in a relative abundance change lower than 10^{-5} for the heavier nuclei and even less for lighter ones. Accounting for baryons at all is questionable, and tracking the abundance of non-thermal electrons and energy changes caused by nucleosynthesis is completely unnecessary. Accordingly, the background variables can be treated as independent of the abundances.

This is beneficial, as unlike the abundances, the equations governing temperature and scale factor are not stiff in the slightest. This allows faster integration with fewer evaluations of computationally demanding terms such as the sum in electron energy density eq. (1.37). Barring $e^- e^+$ annihilation, T and a follow the simple power laws $T^{-2} \propto t$ and $a^2 \propto t$, as seen on figure 1.2. This allows for the use of simple linear interpolation in log space, which will have a negligible impact on runtime compared to the evaluation of reaction rates.

Compared to the background parameters, evaluating reaction rates is quite simple, with the most time-consuming part being the sheer number of rates. Here, the main problem is the aforementioned stiffness, but this is also aided by precomputing the background variables, as this demonstrably improves stability.

2.3 Creating the Reaction Network

To create the reaction network I use `pynucastro`[31], which is an open-source Python interface designed for nuclear astrophysics. The reaction rates themselves are provided by the REACLIB database[15]. The purpose of the REACLIB database itself is to provide the best possible collection of reaction rates based on the current state of scientific knowledge. This provides the best possible basis for a reaction network that is **agnostic** to the biases inherent in rates selected by the same people developing the BBN code. These rates are based on fits of experimental results using the following parametrization

$$\lambda = \exp \left(a_0 + \sum_{i=1}^5 a_i T_9^{\frac{2i-5}{3}} + a_6 \log T_9 \right). \quad (2.2)$$

T_9 is the temperature in 10^9 K, and the associated molar density in eq. (1.58) must be provided in cgs units of mol/cm^3 . Converting from natural units to cgs is a simple matter of multiplying by $\frac{\text{MeV}^3}{\hbar c} \frac{1}{N_0} = 2.161 \times 10^8 \text{ cm}^{-3}$, with N_0 being the Avogadro number. For some reactions, such as those with powerful resonances, a rate can be comprised of multiple terms of the form given in eq. (2.2) to allow for a more accurate fit of the data.

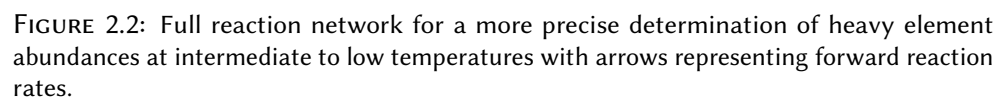
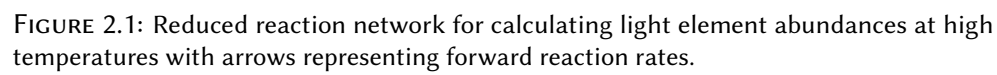
To create the network, `pynucastro` must first be provided with the list of included nuclei. It has a built-in method for collecting all reactions between these nuclei, which creates a library object containing the rates and their relations. This can then be used to generate a Python file that takes density, temperature, and abundances as inputs and returns the RHS and Jacobian. This file supports just-in-time compilation using the JIT module from Numba, which takes between a few seconds to a few minutes, depending on the size of the network. To avoid having to recompile the networks every time I modify the code, I added a method that compiles the network ahead of time using the Numba CC module.

At high temperatures, heavy nuclei have extremely low abundances while greatly increasing the stiffness of the system. To increase both stability and performance, it is prudent to extend the network gradually, which can be accomplished by using three different reaction networks.

At very high temperatures, deuterium is readily destroyed by high-energy photons inhibiting the production of any subsequent nuclei. Here the simplest possible reaction network is employed, comprised of only the proton, neutron, and their forward and reverse rates.

When temperatures are low enough to allow deuterium production, the network is extended to include all nuclei with $A \leq 7$, as seen in figure 2.1. This accounts for the nuclei involved in ${}^4\text{He}$ production as well as their immediate fusion products, which are also the only nuclei with observable final abundances.

When significant amounts of ${}^4\text{He}$ and heavier nuclei have formed, we switch to the full network, which includes every nucleus that could possibly affect BBN, as seen in figure 2.2. Due to the extreme temperature dependence of reactions such as triple-alpha, this network is very stiff at high temperatures.



2.4 Running APODORA

- We use pynucastro to generate the reaction networks. This is by far the most time-consuming step, but unless we need to modify a reaction rate, we only need to do it once.
- The time evolution of background parameters is calculated and stored.
- Initial conditions are set based on the background parameters, with the proton and neutron abundance being determined from NSE.
- The first reaction network is integrated from a specified initial time until the switch to the second network.
- Before beginning integration of the second network, the initial abundance of the added nuclei is determined by requiring that the resulting right-hand-side (RHS) is 0.
- The second reaction network is integrated using these initial conditions, after which the same procedure is used for the third network.
- Barring the addition of additional reaction networks, we get the final abundances, as well as their evolution over time.

Results and Discussion

Running APODORA creates an array with the abundance of every nuclei at each timestep, which are visualized in figure 3.1. In combination with interfaces from pynucastro similar plots can be created for the reaction rates, some of which are shown in appendix A. Based on this, we can make a detailed description of the evolution of early nuclei abundances.

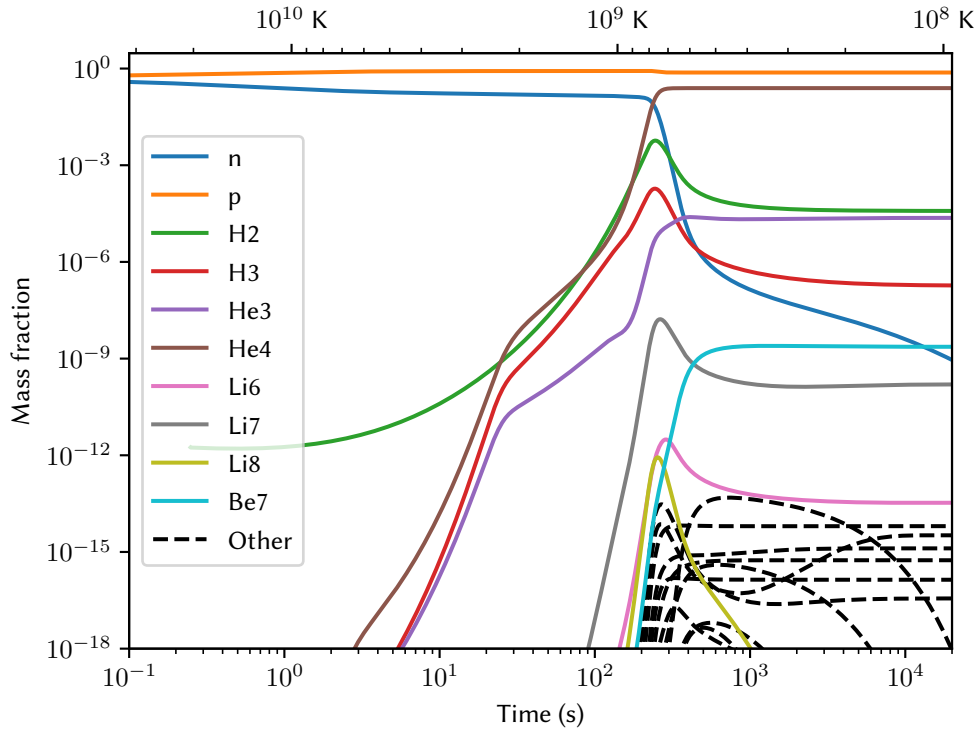


FIGURE 3.1: Time evolution of light nuclei abundance during BBN, with mass fraction technically being the close approximation $X_i = Y_i A_i$. The bottom axis shows the time passed since The Big Bang, and the top axis shows the temperature at this time.

As expected, neutrons, protons, and deuterium remain in equilibrium for the first few seconds. As the temperature decreases, deuterium abundances slowly increase, quickly followed by tritium and both helium isotopes. This continues until around 230 seconds, at which point the rate of ${}^4\text{He}$ creation is finally great enough to have a significant impact on neutron abundance, which until then had remained almost unchanged since the $p \leftrightarrow n$ rates fell out of equilibrium. This leads to a rapid drop in neutron abundance, creating a bottleneck in the production of deuterium and tritium. Without neutron capture to create more, the existing deuterium and tritium is converted to ${}^4\text{He}$ via ${}^3\text{H} + {}^2\text{H} \rightarrow {}^4\text{He} + n$. Without these light nuclei, lithium abundances also drop, as reactions such as ${}^4\text{He} + {}^3\text{H} \rightarrow {}^7\text{Li}$ become outmatched by the proton captures ${}^7\text{Li} + p \rightarrow 2{}^4\text{He}$ and ${}^6\text{Li} + p \rightarrow {}^7\text{Be}$. Conversely, Beryllium 7 is primarily destroyed via neutron capture ${}^7\text{Be} + n \rightarrow {}^7\text{Li} + p$, and therefore sees a rapid increase in abundance immediately after the drop in neutrons.

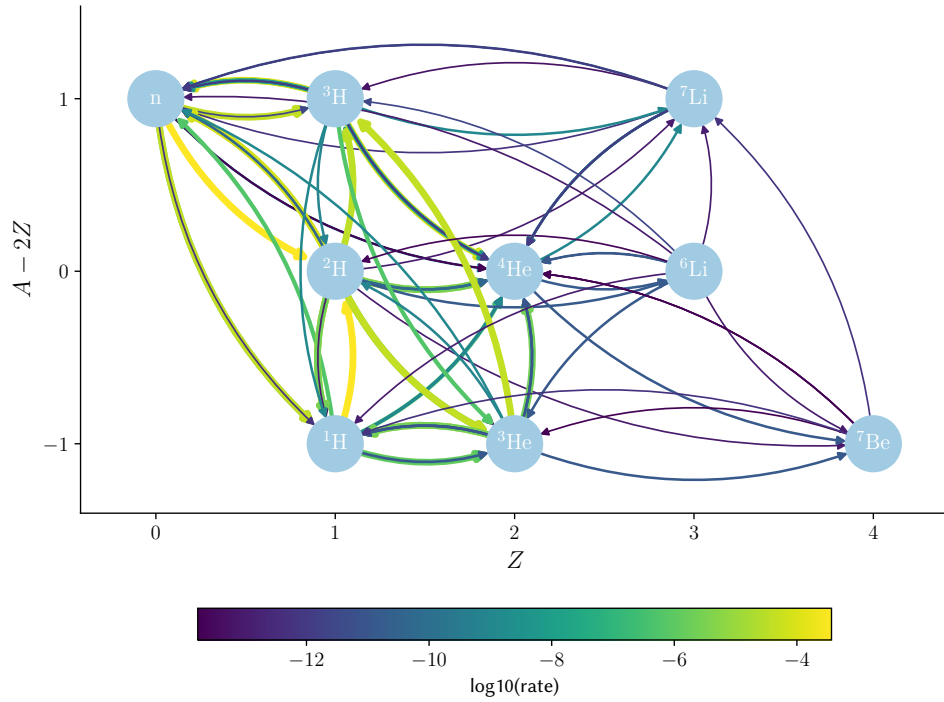


FIGURE 3.2: Reaction rates 5 minutes after Big Bang at $7.6e8$ K. Only including rates within ten orders of magnitude of strongest. The nuclei are located based on atomic number Z , and excess neutrons $A - 2Z$. Each rate is represented by arrows from each reactant to each product, with color and width representing the strength.

The relations of these reactions are illustrated in figure 3.2. This snapshot is taken immediately after the aforementioned drop in neutron abundance with $Y_n = 0.2\%$. Despite this, $n + p \rightarrow d$ is still the strongest reaction rate, followed by rates creating ${}^3\text{H}$ and ${}^3\text{He}$, simply due to the high abundance of these light nuclei. Though no particular reaction is exceptionally strong, a disproportionate amount of reactions produce rather than consume ${}^4\text{He}$. This should come as no surprise as ${}^4\text{He}$ is the most tightly bound of all these nuclei. The only rates consuming helium are those

producing heavier elements, ${}^4\text{He} + {}^3\text{H} \rightarrow {}^7\text{Li}$, ${}^4\text{He} + {}^3\text{He} \rightarrow {}^7\text{Be}$, and ${}^4\text{He} + {}^2\text{H} \rightarrow {}^6\text{Li}$. Yet these barely affect total helium abundance, and to an extent help create more ${}^4\text{He}$ through subsequent reactions such as ${}^7\text{Li} + {}^2\text{H} \rightarrow 2{}^4\text{He} + \text{n}$.

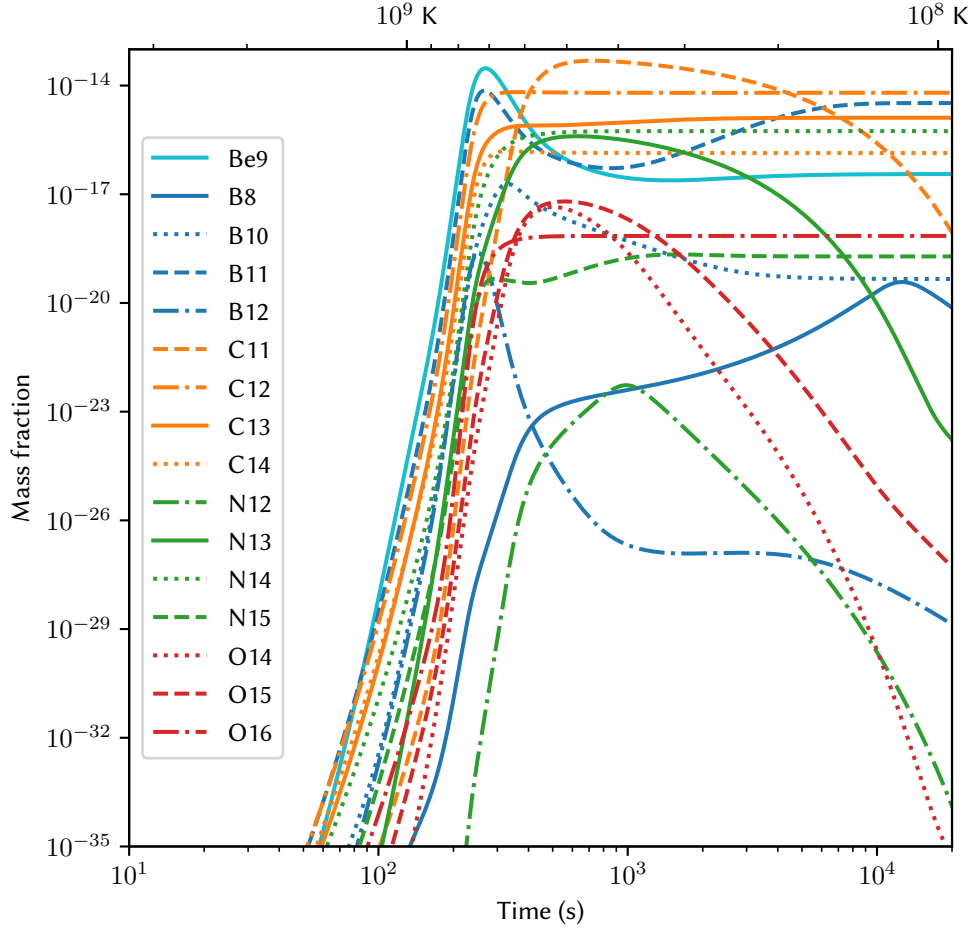


FIGURE 3.3: Time evolution of heavy nuclei abundance during BBN, with mass fraction technically being the close approximation $X_i = Y_i A_i$. The bottom axis shows the time passed since The Big Bang, and the top axis shows the temperature at this time.

The most striking effect of the high ${}^4\text{He}$ binding energy is the lack of stable nuclei with $A = 8$, due to two alpha particles being energetically favorable. Many nearby nuclei are also unstable, creating a gap in the full reaction network, apparent on 2.2. The next nucleus with greater binding energy per nucleon is ${}^{12}\text{C}$, which, after BBN, is also the most abundant of the heavy nuclei, as seen in figure 3.3. Bridging the gap between ${}^4\text{He}$ and ${}^{12}\text{C}$ is usually accomplished via the triple-alpha process $3{}^4\text{He} \rightarrow {}^{12}\text{C}$, which occurs in stars at temperatures above 10^8K . The temperature during BBN is even higher than this, but compared to stellar interiors, the density is much lower. At the previously mentioned 5-minute mark, the baryon density of the universe is only 10 grams per cubic meter, which is more than ten orders of magnitude lower than that of a helium burning stellar core. This completely stops the triple-alpha process, leaving the inefficient process of alpha capture on ${}^7\text{Li}$ and

later ${}^7\text{Be}$ as the only options for creating heavier nuclei. This firstly creates ${}^{11}\text{B}$, which, through proton capture, is responsible for the majority of ${}^{12}\text{C}$ production. Unfortunately, the resulting excited state ${}^{12}\text{C}^*$ predominately decays into three alpha particles, with the branching ratio of internal transition into the ground state being only 1.5×10^{-4} . The same is true for neutron capture on ${}^{11}\text{C}$, though it also decays via proton emission ${}^{12}\text{C}^* \rightarrow {}^{11}\text{B} + \text{p}$ and of course freely decays ${}^{11}\text{C} \rightarrow {}^{11}\text{B}$. From figure 3.3 we also see an initial bump in ${}^9\text{Be}$ abundance caused by the uniquely high cross-section of the reaction ${}^7\text{Li} + {}^3\text{H} \rightarrow {}^9\text{Be} + n$, but as tritium abundance drops most ${}^9\text{Be}$ is destroyed by photofission $\gamma + {}^9\text{Be} \rightarrow 2{}^4\text{He} + n$.

3.1 Accuracy

Throughout the code, there are several places where numerical **accuracy** must be balanced by the need for swift computation. As a baseline, I aim for a relative precision on final abundances of 10^{-5} due to numerical uncertainty. This is much lower than the error introduced by the experimental determination of reaction rates, as well as that of astronomical observations of primordial abundances, which will be covered in sections 3.2 and 3.3.

3.1.1 Tolerances

For the integration itself, I use the `solve_ivp` method from `scipy.integrate`[25]. Here, the relative and absolute tolerances must be specified as optional parameters to ensure the desired numerical accuracy. We start with the background parameters, for which only the relative tolerance matters since the temperature and scale factor must be precise no matter their absolute value. So, by setting the absolute tolerance to 0, we can plot the error caused by relative tolerance. From figure 3.4 it appears that the resulting error in final abundances is between one and two orders of magnitude greater than the error in background parameters. The majority of this error is not random and seems to be caused by the lower tolerance consistently leading to a lower baryon density, as evident from the fact that ${}^7\text{Be}$ decreases as opposed to most other nuclei (fig. 3.15). To achieve the desired accuracy of 10^{-5} , the relative tolerance for background should be set at 10^{-7} .

For the relative tolerance of the network, it is much more straightforward. Unsurprisingly, there is a one-to-one correspondence between the relative tolerance and resulting error, as seen in figure 3.5. However, this is only true for the greatest outliers among the heavy nuclei. For the relevant light nuclei, the deviation is much smaller, and a relative tolerance of 10^{-4} should be sufficient to achieve the desired precision.

From figure 3.6, we see that the absolute tolerance only affects nuclei when they get close to their final abundance. Therefore, the absolute tolerance can be set at 10^{-20} if accurate heavy nuclei abundance is needed, and 10^{-15} if only light nuclei are desired.

3.1.2 Electron Energy

Most calculations for the background have nice analytical expressions that can be computed with arbitrary precision. The electron energy density is the main exception,

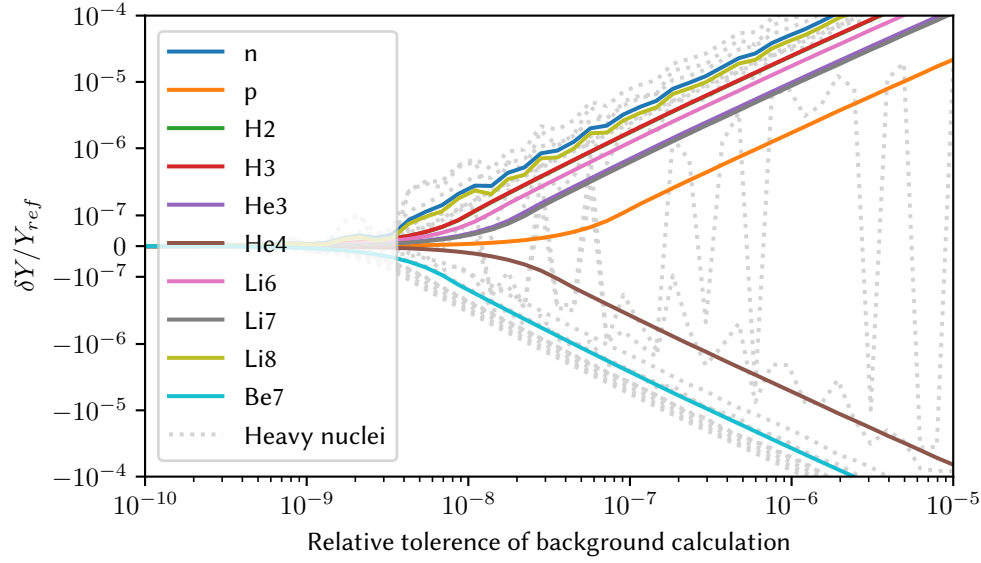


FIGURE 3.4: Relative deviation on final abundances based on the relative tolerance used for determining background variables. Plot is linear in the region $[-10^{-7}, 10^{-7}]$ and logarithmic outside.

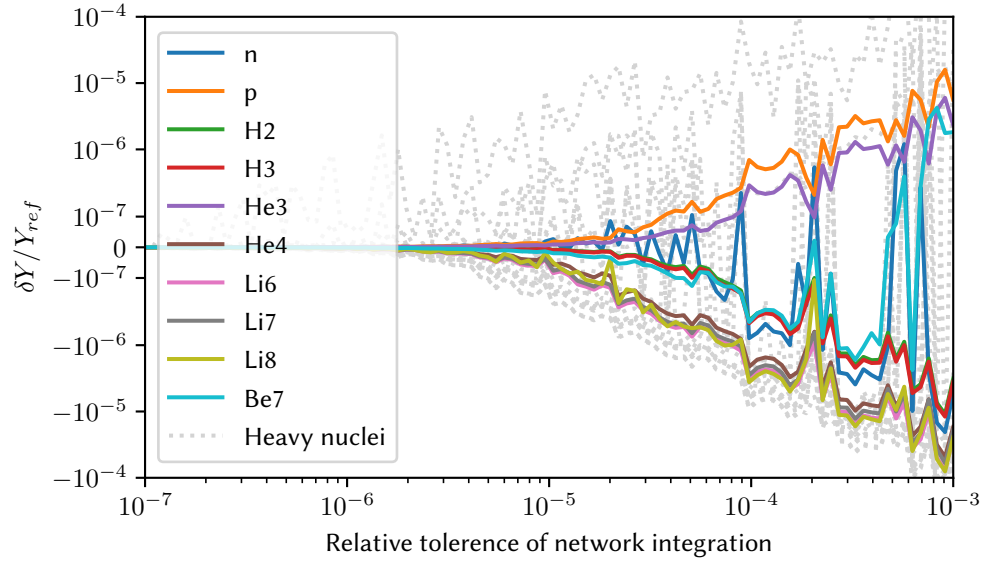


FIGURE 3.5: Relative deviation on final abundances based on the relative tolerance of the network integration. Plot is linear in the region $[-10^{-7}, 10^{-7}]$ and logarithmic outside.

as it is given by an infinite sum (1.37) of which a finite number of terms must be calculated. Electrons annihilate very early, so any error in the energy density will only affect the $p \rightleftharpoons n$ rate. This will lead to a small change in neutron abundance, which results in a similar (within one order of magnitude) relative change in the abundance of all subsequent nuclei. Testing shows that small changes to the energy density cause a change in neutron abundance of roughly the same relative magnitude,

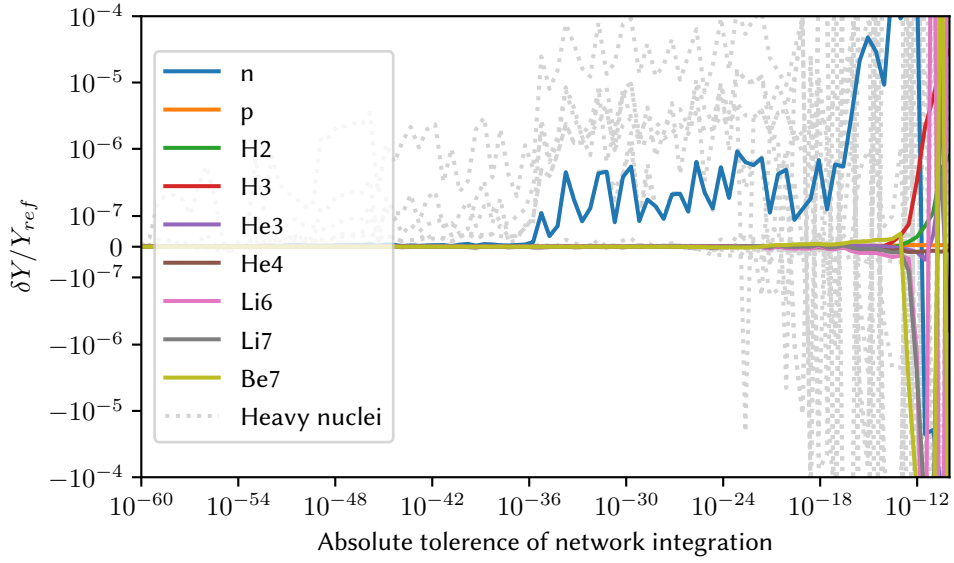


FIGURE 3.6: Relative deviation on final abundances based on the absolute tolerance of the network integration. Plot is linear in the region $[-10^{-7}, 10^{-7}]$ and logarithmic outside.

if not slightly lower. So, to achieve the requested accuracy in abundance, I also aimed for a 10^{-5} relative error in total energy density.

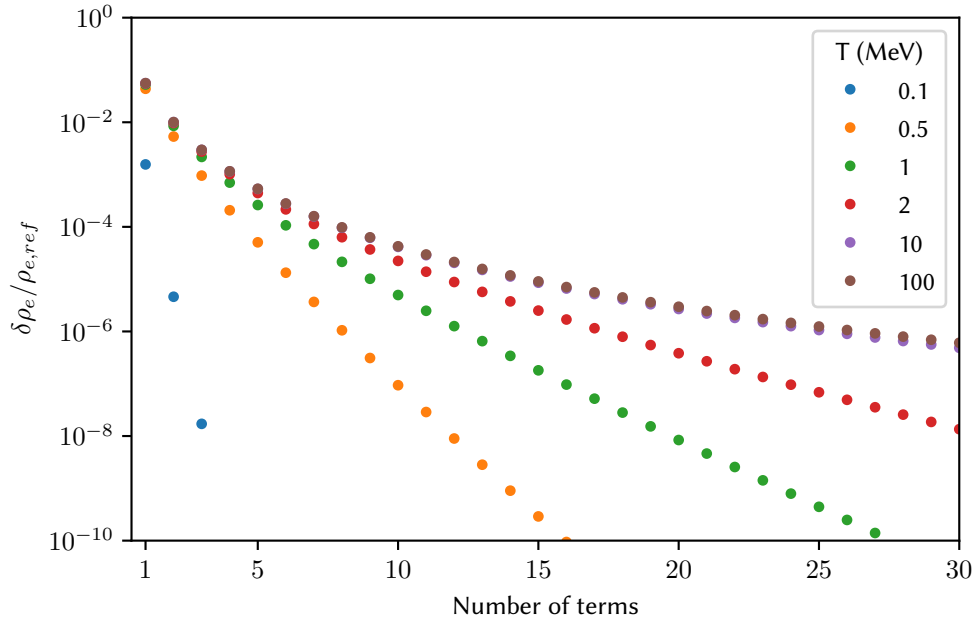


FIGURE 3.7: Normalized absolute deviation of electron energy density from the reference energy as a function of included terms in (1.37). The reference energy density has been determined by computing the first 10000 terms.

Figure 3.7 shows the deviation from the reference energy at select temperatures before and during $e^- e^+$ annihilation. For low temperatures, the sum converges

quickly, which should come as no surprise as the series in (1.32), converges more rapidly as $e^{-(E \pm \mu)/T}$ approaches 0. At high temperatures, the sum converges at a much slower rate, but it still achieves sufficient accuracy with only 20 terms.

3.1.3 Interpolation

For the interpolation of background variables, an appropriate number of points must be selected. These points are spaced uniformly in $\log(t)$. Tests show that 10^4 points are sufficient to achieve the required accuracy in final abundances. However, a low number of points causes small discontinuities in the derivatives of temperature and scale factor. Due to the stiffness of the system, this leads to instabilities, which have a major impact on the runtime. At the required resolution of 10^4 the integration routine has to make twice as many calls to the RHS, compared to smoother integration. At 2×10^5 points, the interpolation is smooth enough to not cause issues for integration.

3.1.4 Network Timings

As mentioned in section 2.3, we cannot calculate the abundance of all nuclei from the beginning and instead have to add them gradually as they become relevant. To find this point, we can plot the deviation in final abundance as a function of the time at which we switch between networks.

Full Network

We start by looking at the full network shown in figure 3.8, which shows how groups of nuclei start to deviate at three distinct points. As long as the heavy nuclei are added before the 2-minute mark corresponding to $T > 10^9\text{K}$, they have time to reach the same abundance as they would if they were added earlier. Adding them later will delay the initial production, which will slowly lower the resulting final abundance. They will, however, still reach approximately the same final abundance until the late stages of BBN at around 7 minutes. Here, the temperature will be too low for their formation, resulting in an increase in Lithium and Beryllium, as these are no longer consumed to produce heavy nuclei. The reactions involving ^{11}C , however, come into effect much later than most other reactions and remain relevant even an hour after BBN. If ^{11}C is added after this point, it will never achieve a significant final abundance, leading to a drop in its indirect daughter nuclei ^9Be and ^6Li .

The result of this test shows that for standard BBN, heavy nuclei don't actually need to be included at all if one is only interested in the abundances of light nuclei. For completeness, I will choose to include these nuclei anyway, starting at $T > 10^9\text{K}$.

Light Network

From figure 3.9, we see that delaying the calculation of nuclear abundances initially causes an increase in the abundance of protons and the proton-dominated nuclei ^3He and ^8B , with all other abundances dropping. This is due to early nuclear reactions trapping neutrons in the cores of light nuclei such as ^4He and ^2H , preventing their free decay into protons. However, since the vast majority of neutrons are still unbound, this effect will be insignificant until large light nuclei abundances are

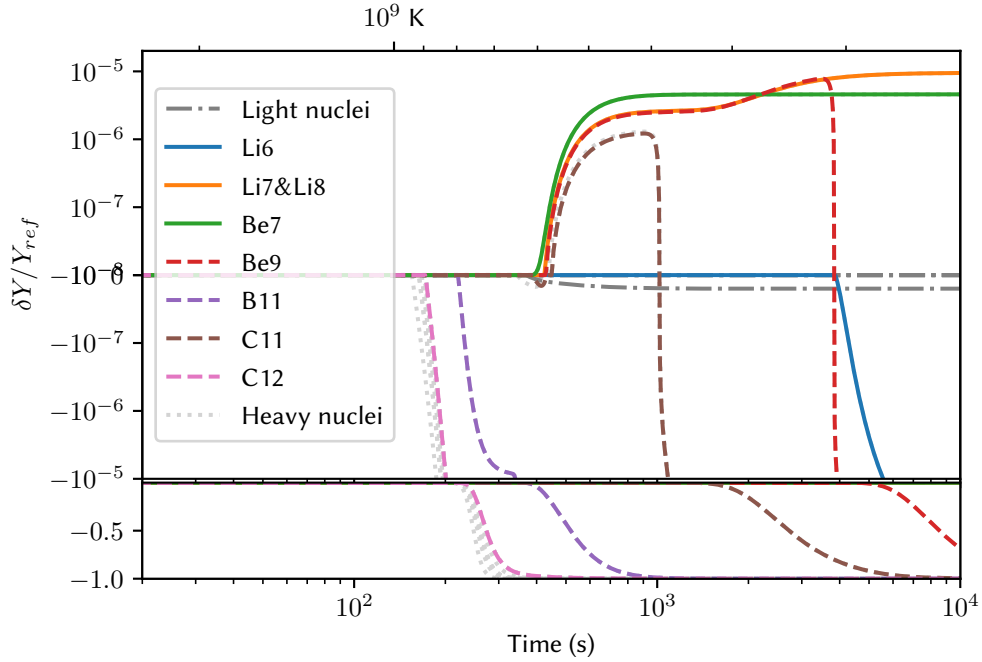


FIGURE 3.8: Relative deviation on final abundances based on the time from which heavy nuclei are included in the reaction network. To display both positive and negative changes, relative deviations $< 10^{-8}$ are excluded. The bottom shows negative deviation on a linear scale.

attained. Therefore, we actually don't need to calculate early abundances to get precise estimates of the final abundance.

Not having to solve the reaction network at high temperatures makes the system much less stiff, potentially allowing future BBN codes to use less complex integration routines than those used by this and older codes. Unfortunately, starting abundance calculations presents a major issue due to the initial conditions. When starting light abundance calculation at early times $t < 10$ s, we can determine the initial abundances by setting the RHS to 0 as described in section 2.4. But at later times, reactions destroying ${}^4\text{He}$ drop off, with ${}^4\text{He}$ abundances instead being kept in check by the lack of deuterium. As the system is no longer in exact NSE, any method for determining initial conditions that assume a steady-state solution will fail. Given enough time, all neutrons will be converted to ${}^4\text{He}$, and the estimated initial conditions reflect this by vastly overestimating ${}^4\text{He}$ abundances. To get around this and produce figure 3.9, I instead had to set all initial abundances to 0 when initiating the light network after 3 seconds. This workaround eliminates the problem but creates another in the form of transients, which are created as abundances go from 0 to their appropriate value. Since the system of equations is less stiff at these late times, the transients won't break the integration. But dealing with these transients takes just as long as the time required for tracking abundances at early times.

$p \rightleftharpoons n$ Network

Unlike the heavier nuclei, the time at which we start calculating neutron and proton abundances has a very abrupt and significant impact on final abundances. As long as

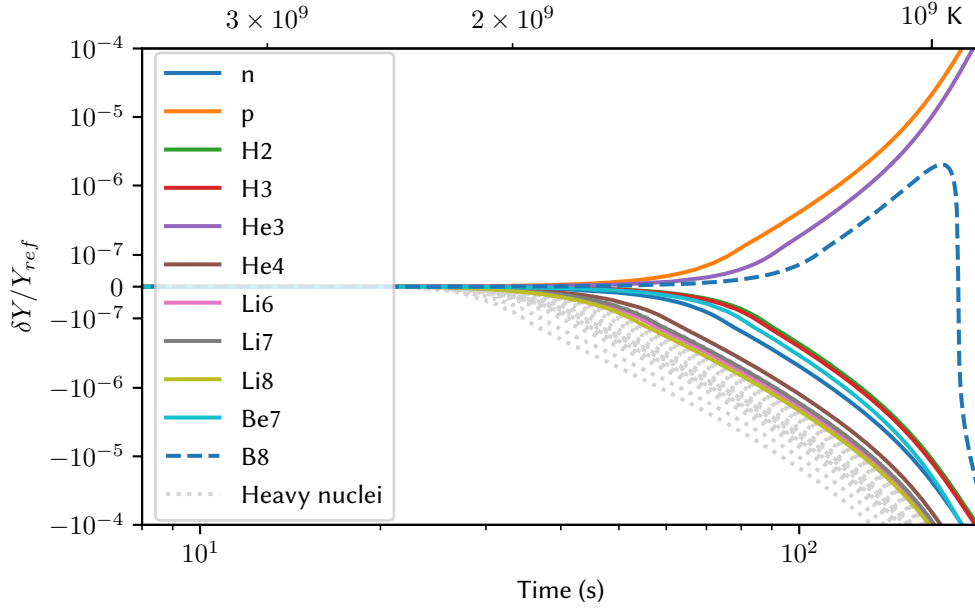


FIGURE 3.9: Relative deviation on final abundances based on the time from which light nuclei are added to the reaction network. Plot is linear in the region $[-10^{-7}, 10^{-7}]$ and logarithmic outside.

they are still in thermal equilibrium when we begin calculations, the final abundance will be the same. Conversely, if we start after they begin to fall out of thermal equilibrium, all final abundances will be radically different. From figure 3.10, it's clear that this occurs at around 100 ms or $T = 3 \times 10^{10}$ K, and as long as we initiate $p \rightleftharpoons n$ before this we get precise results. This also justifies the use of $T = 27 \times 10^9$ K as the initial temperature, which is the point used by, among others, Wagoner, Kawano, and ALTERBBN.

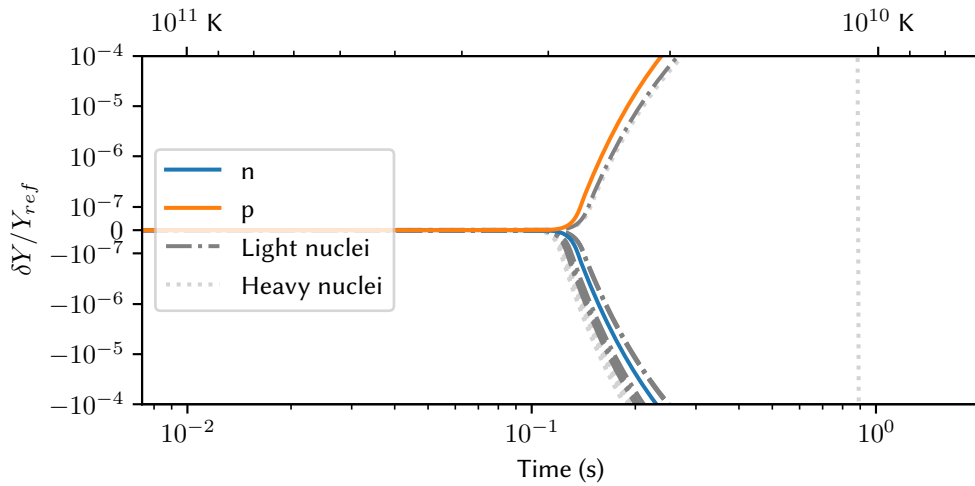


FIGURE 3.10: Relative deviation of final abundances based on the initial time of BBN calculations. Plot is linear in the region $[-10^{-7}, 10^{-7}]$ and logarithmic outside.

3.1.5 Neutrino Decoupling

The main source of inaccuracy in APODORA is the assumption of complete neutrino decoupling. This assumption is reasonable as the only net transfer of energy between different particles is the annihilation of electrons and positrons, which begins at around 1 MeV, as shown in figure 1.1. At this point, neutrinos have mostly decoupled, and therefore, the energy is transferred to the photons, which are heated relative to the neutrinos by the well-known factor $\sqrt{11/4}$. However, there is a small transfer of energy before the neutrinos completely decouple from the other particles. The result of this is a small increase in neutrino energy density relative to photon energy of around 1% [9]. As both neutrinos and photons are ultrarelativistic, this change is inconsequential to the time evolution of the early universe, and therefore, one might assume that it would not have a significant impact on final abundances. This, however, is not the case, as is apparent from figure 3.11. The reason for this is that the higher photon temperature caused by instantaneous decoupling effectively delays the onset of nucleosynthesis since the baryons take longer to cool sufficiently. This has two main effects, the first being slightly lower baryon density at any given temperature, and the second that the universe will remain in any given temperature range for longer. Additionally, neutrino decoupling also affects the $p \rightleftharpoons n$ reactions directly, as these rely on both the exact temperature and non-thermal energy distribution of the neutrinos. When assuming complete neutrino decoupling, these effects lower the abundance of ${}^4\text{He}$ by 0.05%, ${}^3\text{He}$ by 0.1%, and deuterium by 0.5%, and increase ${}^7\text{Be}$ by 0.5%, (PRIMAT table V[21]).

As mentioned in section 1.2.3, we can compensate for this by using an effective neutrino number $N_\nu^{\text{eff}} = 3.045$, to account for the transferred energy. Yet, this was implemented when producing figure 3.11, which still shows deviations characteristic of an altered T_ν/T_γ ratio. This is due to N_ν^{eff} effectively adding additional energy to the universe, which causes the universe to expand more rapidly, cooling the neutrinos. Secondly, the electrons and positrons are not completely relativistic, which causes the temperature of coupled components to not scale exactly with a^{-4} . To reduce the deviation in the T_ν/T_γ ratio, we can decouple the neutrinos as close as possible to the point at which they actually decouple. This still assumes an instant rather than gradual decoupling but nonetheless improves predicted abundances. The point at which neutrinos decouple obviously coincides with the freezeout of $p \rightleftharpoons n$ reactions, and as shown on 3.10, we can safely begin both background and network integration at 27 GK corresponding to 2.3 MeV. From table 3.1, we clearly see

	$Y_p \times 10$	${}^2\text{H} \times 10^5$	${}^3\text{He} \times 10^5$	${}^7\text{Li} \times 10^{10}$	${}^6\text{Li} \times 10^{15}$	${}^7\text{Be} \times 10^{10}$
100 MeV	2.470	2.532	1.040	4.712	7.503	4.411
2.3 MeV	2.472	2.536	1.040	4.706	7.523	4.404
Deviation	0.07%	0.15%	0.04%	-0.15%	0.25%	-0.18%

TABLE 3.1: Comparison of final abundances for instant decoupling at 2.3 and 10 MeV, with all abundances except ${}^4\text{He}$ (Y_p) being normalized to H abundance. ${}^3\text{He}$ and ${}^7\text{Li}$ including contribution from eventual decay of ${}^3\text{H}$ and ${}^7\text{Be}$.

the impact of neutrino decoupling. Compared to the expected changes determined by PRIMAT[21], we see an increased impact on ${}^4\text{He}$ and a reduced impact on ${}^7\text{Be}$

and ${}^3\text{He}$. This can mostly be explained by the $p \rightleftharpoons n$ reactions not being directly impacted in my implementation. The direct effect on $p \rightleftharpoons n$ increases the neutron abundance and subsequently, the abundance of all other nuclei, counteracting the effects on everything but ${}^7\text{Be}$, as well as ${}^3\text{He}$ since its abundance actually increases as neutron abundance drops.

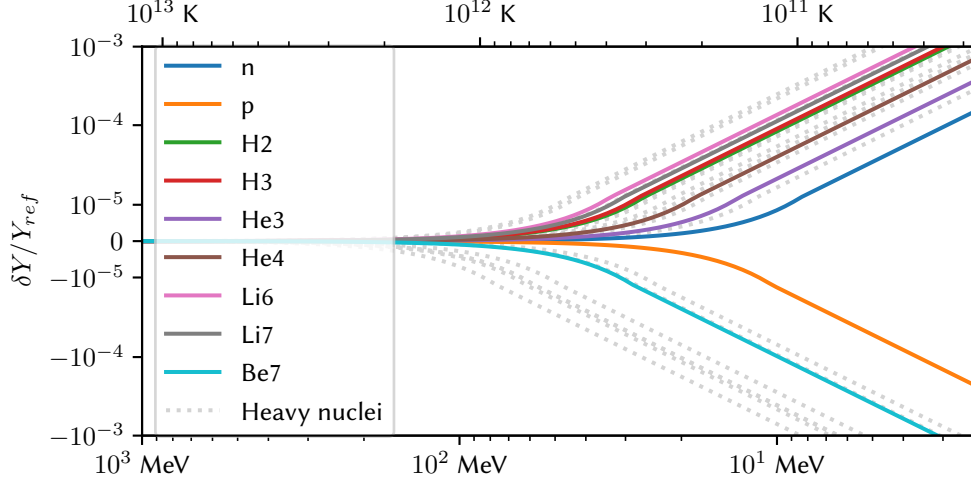


FIGURE 3.11: Relative deviation on final abundances based on the initial time for background calculations. By construction, the initial time coincides with the time of neutrino decoupling.

Though the errors associated with neutrino decoupling are much greater than the achieved numerical error of less than 10^{-5} , they are still acceptable since they are completely inconsequential next to the uncertainty associated with reaction rates, as will become apparent in the following section.

3.2 Comparison with ALTERBBN

To compare the results of APODORA to that of other contemporary BBN codes, I have chosen ALTERBBN. The main reason for this is that it is more accessible than the other two, with the code being directly available on GitHub while not requiring a Mathematica license like PRIMAT. PARTHENOPE would also be a fine choice, but it uses $z = m_e/T$ as the integration variable rather than time. As a result, it would be difficult to perform the one-to-one comparisons in the following sections. Additionally, both APODORA and ALTERBBN use natural units for the background calculations and cgs units for the reaction network. This makes direct comparison of numerical values easier as the only conversion required is an occasional factor of 10^3 due to the energy being measured in GeV rather than MeV.

3.2.1 Speed

As ALTERBBN is written purely in C, it unsurprisingly runs faster than my Python implementation, despite the "outsourcing" of the reaction network. Using WSL and GCC-11.3 on an Intel i3-1115G4 @ 3.00GHz, I get an average runtime of 0.61 seconds, of which 0.33 seconds are for the background calculation and 0.28 seconds for the

network integration. This is slightly slower than the 0.38 seconds for the default routine of ALTERBBN. However, the integration method of ALTERBBN sacrifices accuracy for speed, with the default method causing numerical deviation on final abundances of up to 0.4%. ALTERBBN can employ alternate methods for more accurate results, but these have a major impact on runtime. To achieve the same numerical accuracy as this implementation, we must use the most precise integration method in ALTERBBN, which takes 53.91 seconds. So if numerical consistency above 10^{-3} is required, this implementation is much faster despite being implemented in Python rather than C. Based on this, the requirement of **Alacrity** has been fulfilled.

3.2.2 Predicted Abundances

	$Y_p \times 10$	$^2\text{H} \times 10^5$	$^3\text{He} \times 10^5$	$^7\text{Li} \times 10^{10}$	$^6\text{Li} \times 10^{14}$	$^7\text{Be} \times 10^{10}$
APODORA	2.472	2.536	1.040	4.706	0.752	4.404
ALTERBBN	2.474	2.467	1.034	5.363	1.087	5.075
+/-	0.003	0.038	0.016	0.352	1.085	0.343

TABLE 3.2: Abundances from APODORA and ALTERBBN, with all abundances except ^4He (Y_p) being normalized to the H abundance. ^3He and ^7Li including contribution from eventual decay of ^3H and ^7Be . Quoted uncertainties are those determined by ALTERBBN.

Comparing the final abundances predicted by APODORA and ALTERBBN we see major discrepancies. Most of these are within the uncertainties calculated by ALTERBBN based on the uncertainty of the reaction rates. ^7Be and subsequently ^7Li deviate by more than twice what is predicted, and the same is true for deuterium. To discover the cause of this, we can do a 1 to 1 comparison of the time evolution of the universe according to APODORA and ALTERBBN. Here we use the exact same initial conditions of $T = 27 \times 10^9 \text{K}$, $\eta = 6.1 \times 10^{-10}$ and $\tau_n = 880.2 \text{s}$, remembering to correct for the inaccurate initial time in ALTERBBN as explained in section 1.4.2.

3.2.3 Background

To rule out cosmological differences, we can compare the predicted background parameters from ALTERBBN and APODORA, displayed in figure 3.12. Unsurprisingly, after the common initial temperature of 27GK, ALTERBBN sees a relative increase in neutrino temperature due to incomplete neutrino decoupling. The photon temperature initially decreases more slowly since this term is identical for both codes. But this will also begin to slowly drop, due to the difference in energy transfer. Later there is a small additional drop in photon temperature coinciding with the onset of primary nucleosynthesis. This can be explained by ALTERBBN taking into account the effect of nucleosynthesis on photon temperature due to the energy release of nucleosynthesis. However, the observed effect is unphysical and must be due to numerical errors since the energy release is nowhere near the amount required for an impact on photon temperature of this size, and additionally, it should serve to increase rather than decrease the photon temperature. Lastly, there is a relative decrease of the ALTERBBN neutrino temperature at late times. This is due to ALTERBBN taking into account both baryon and dark matter energy density, which I

have omitted since it clearly doesn't have a significant impact during the era of BBN.

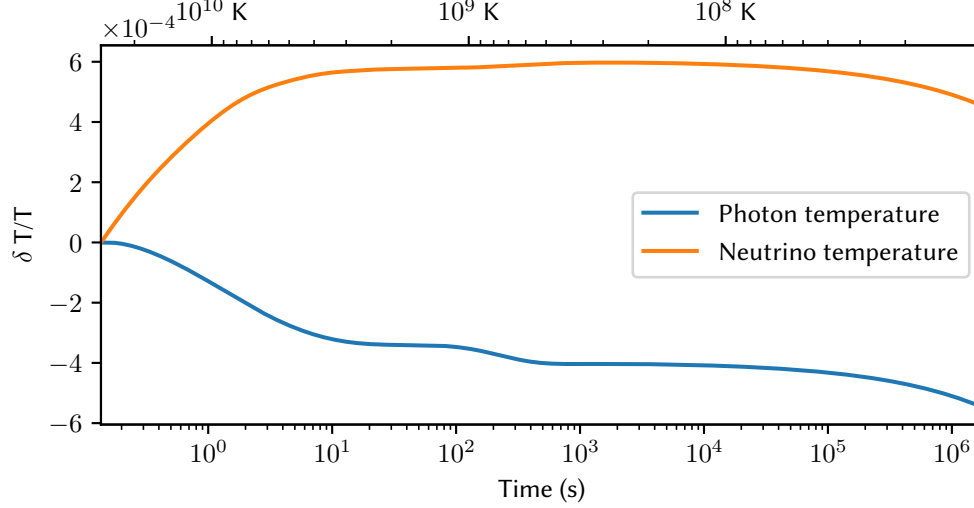


FIGURE 3.12: Relative deviation of temperatures as calculated by APODORA and ALTERBBN. Positive values signify higher ALTERBBN temperatures compared to APODORA.

To see the impact of these background differences, we can integrate the reaction network using the background parameters from ALTERBBN. At its highest precision setting, ALTERBBN takes 64421 discrete time steps, which, based on the test in section 3.1.3 is sufficient to achieve high accuracy with the existing interpolation routine. ALTERBBN does, however, not directly track the scale factor, so we must instead track the baryon density using the neutrino temperature. Since the tabulated $p \rightleftharpoons n$ rates used in this network only depend on temperature, we don't need to know the exact value of n_b before the other reactions become relevant at around 100 seconds, (figure 3.9). At this time, neutrinos have actually decoupled completely, and therefore the relation $T_\nu \propto a^{-1}$ holds exactly. This allows the baryon number density to be determined by $n_b = C \cdot T_\nu^3$ with the constant C being set by requiring $\eta = 6.1 \times 10^{-10}$ at late times.

	$Y_p \times 10$	$^2\text{H} \times 10^5$	$^3\text{He} \times 10^5$	$^7\text{Li} \times 10^{10}$	$^6\text{Li} \times 10^{14}$	$^7\text{Be} \times 10^{10}$
100 MeV	2.470	2.532	1.040	4.712	0.750	4.411
2.3 MeV	2.472	2.536	1.040	4.706	0.752	4.404
APODORA using ALTERBBN T_γ & T_ν	2.473	2.540	1.041	4.699	0.754	4.398
ALTERBBN	2.474	2.467	1.034	5.363	1.087	5.075
+/-	0.003	0.038	0.016	0.352	1.085	0.343

TABLE 3.3: Comparison of final abundances for various background parameters. Showing results of this network using early and late instant neutrino decoupling, as well as the ALTERBBN background which accounts for incomplete decoupling. The last row shows result from the ALTERBBN background using their own abundance calculations.

The result of using the background parameters of ALTERBBN are displayed in Table 3.3. Though somewhat obscured by the lack of significant digits, the relative

change caused by using the ALTERBBN background is equal to 90% of the change caused by changing the timing of instant neutrino decoupling. This is due to the increase in T_ν/T_γ predicted by full incomplete decoupling, being 1.9 times greater than what is achieved by simply delaying instant decoupling. ${}^4\text{He}$ however only increases by 68% of that caused by delayed decoupling. This is due to ${}^4\text{He}$ being governed by the $p \rightleftharpoons n$ reactions, which take place while T_ν/T_γ is still increasing. This supports the previous assumption that the only major difference between the cosmological calculation of ALTERBBN and APODORA is their inclusion of incomplete neutrino decoupling.

3.2.4 Reaction Network

Since the difference in background introduces minimal abundance corrections, the discrepancy between the ALTERBBN results and mine must unsurprisingly be due to differences in the reaction network. To see where these differences are, we can plot the relative difference between abundances as they evolve during BBN, displayed in figure 3.13.

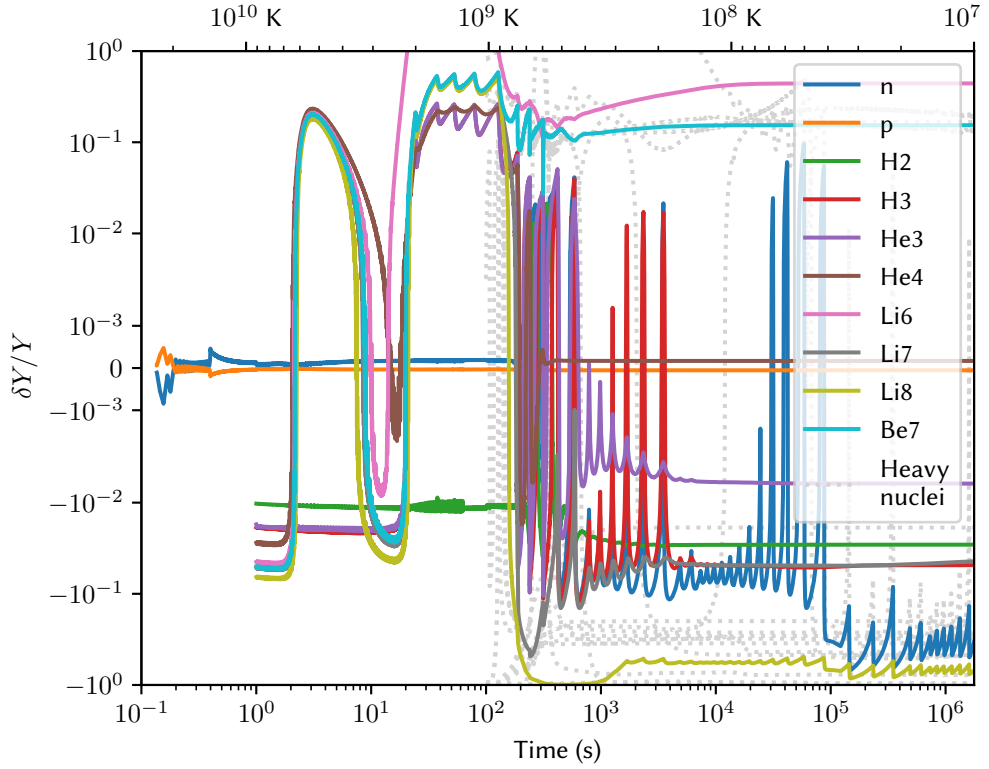


FIGURE 3.13: Relative deviation on abundances between APODORA and ALTERBBN, during the various stages of BBN. To rule out cosmological differences, the ALTERBBN background parameters are used for both calculations. Plot is linear in the region $[-10^{-3}, 10^{-3}]$ and logarithmic outside.

Starting at the high-temperature limit, we see how the differences in early $p \rightleftharpoons n$ rates cause a deviation in proton and neutron abundance. This deviation

corresponds exactly to that of the final ${}^4\text{He}$ abundance. We can therefore conclude that the difference in Y_p is purely due to differences in this rate.

The next notable difference is the relative increase and subsequent drop in ${}^4\text{He}$ abundances, which takes place between 2 and 20 seconds. This matches the time period where in which the relative strength of the ${}^3\text{He} + n \rightarrow {}^4\text{He}$ rate is greatest compared to that of other reactions for ${}^4\text{He}$ production. Suspecting this particular reaction is further supported by ALTERBBN using a linear approximation for the rate, stemming from the original Wagoner code[5]. Though inaccurate, this doesn't actually have a significant impact on final abundances since the reaction only dominates ${}^4\text{He}$ production at very early times.

Following this, we see the most striking features, which are the periodic spikes in relative abundance affecting almost every single nuclei. This jaggedness originates in ALTERBBN and is caused by their implementation of certain reaction rates. As described in section 2.3, I use smooth fits of experimental data to obtain appropriate values for the reaction rates at any temperature. With every one of these rates stemming from the most recent snapshot of the REACLIB database[15] available in pynucastro[31]. ALTERBBN on the other hand, uses a manually curated list of reaction rates, with a myriad of different sources and implementations. A few of these rates are tabulated, and to obtain values between the tabulated temperature steps, ALTERBBN simply uses nearest-neighbor interpolation. This is hard-coded as a series of consecutive else/if statements, which return the value of the reaction rate in discreet steps according to the nearest tabulated value. The spikes happen whenever these rates assume a new value. As an example ALTERBBN uses a tabulated ${}^2\text{H} + p \rightarrow {}^3\text{He}$ rate from Coc et al. [17], which is responsible for the small early spikes in ${}^3\text{He}$, and other nuclei that depend on its abundance. This can be confirmed by noting that the early spikes peak at 1.875, 1.625, 1.375, and 1.125 GK, which happen to be the exact midpoints between the tabulated values, which are at 2, 1.75, 1.50, 1.25, and 1 GK.

These spikes obscure what processes are responsible for the deviation in nuclear abundances, but for ${}^7\text{Li}$ and ${}^7\text{Be}$ in particular, we can make very good guesses as to what these reactions are. The primary reactions responsible for creating and destroying ${}^7\text{Li}$ are ${}^3\text{H} + {}^4\text{He} \rightarrow {}^7\text{Li}$ and ${}^7\text{Li} + p \rightarrow {}^4\text{He}$, with ${}^7\text{Be}$ being governed by ${}^3\text{He} + {}^4\text{He} \rightarrow {}^7\text{Be}$ and ${}^7\text{Be} + n \rightarrow {}^7\text{Li} + p$. Compared to these, all other reactions are completely insignificant, which can be seen on figs. A.9 to A.12. This makes these reactions the most likely cause of the deviations, which is further supported by ALTERBBN and my network using different rates for each one of them.

3.2.5 Modifying the Network with AlterBBN rates

To test these claims, we can replace the default rates in my network with the four ${}^7\text{Li}$ and ${}^7\text{Be}$ rates from ALTERBBN as well as the previously mentioned ${}^3\text{He} + n \rightarrow {}^4\text{He}$ rate. Due to the modular nature of my reaction network, this is quite easy to accomplish, with the resulting abundances being shown on table 3.4. As expected, only the abundances of ${}^7\text{Li}$ and ${}^7\text{Be}$ are affected since the total abundances of light nuclei involved in the four reactions are much higher.

Though the modified rates bring ${}^7\text{Li}$ and ${}^7\text{Be}$ abundances within the estimated uncertainty of ALTERBBN, they still deviate significantly. To explain this, figure

	$Y_p \times 10$	$^2\text{H} \times 10^5$	$^3\text{He} \times 10^5$	$^7\text{Li} \times 10^{10}$	$^6\text{Li} \times 10^{14}$	$^7\text{Be} \times 10^{10}$
Default rates	2.473	2.540	1.041	4.699	0.754	4.398
Rates from ALTERBBN	2.473	2.540	1.041	5.133	0.754	4.837
ALTERBBN +/-	2.474 0.003	2.467 0.038	1.034 0.016	5.363 0.352	1.087 1.085	5.075 0.343

TABLE 3.4: Final abundances for the default APODORA network, the network using select ALTERBBN rates, and the results from ALTERBBN.

3.13 can be recreated using the modified reaction network, resulting in figure 3.14. Looking at the early abundances, we confirm that the initial difference in light nuclei abundance was indeed caused by the $^3\text{He} + n \rightarrow ^4\text{He}$ rate. Additionally, we see how the spiking affects both ^7Li and ^7Be right up until the point at which they settle into their final abundances, making this the most likely explanation for the remaining discrepancy.

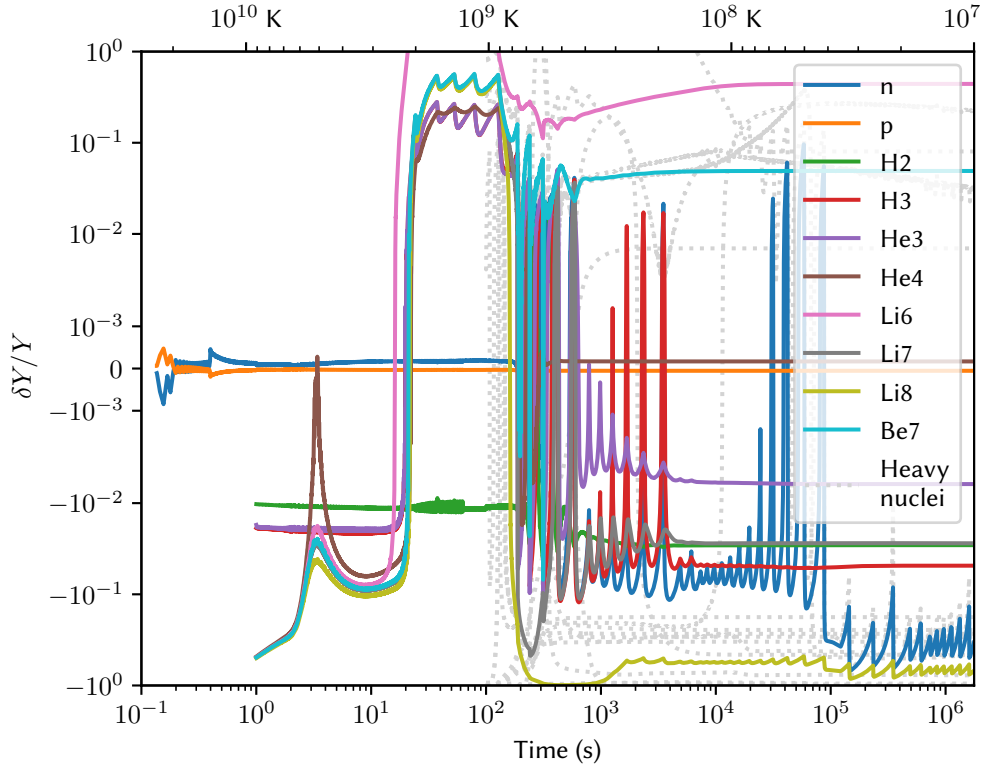


FIGURE 3.14: Same as fig. 3.13, but with the network using the same rates as ALTERBBN for the reactions $^3\text{He} + n \rightarrow ^4\text{He}$, ^7Li are $^3\text{H} + ^4\text{He} \rightarrow ^7\text{Li}$, $^7\text{Li} + p \rightarrow ^4\text{He}$, $^3\text{He} + ^4\text{He} \rightarrow ^7\text{Be}$, and $^7\text{Be} + n \rightarrow ^7\text{Li} + p$.

3.3 Final Abundances

With differences between APODORA and ALTERBBN established, we can look at the correlation with the other codes and, more importantly, the actual observations.

From table 3.5, we see how the abundances predicted by APODORA lie within the

	$Y_p \times 10$	$^2\text{H} \times 10^5$	$^3\text{He} \times 10^5$	$^7\text{Li} \times 10^{10}$
Observations	2.453 ± 0.034	2.527 ± 0.030	$< 1.1 \pm 0.2$	1.6 ± 0.3
APODORA	2.472	2.536	1.040	4.706
ALTERBBN	2.474 ± 0.003	2.467 ± 0.038	1.034 ± 0.016	5.363 ± 0.343
PRIMAT	2.4709 ± 0.0017	2.459 ± 0.036	1.074 ± 0.026	5.623 ± 0.247
PARTHENOPE	2.4687 ± 0.0012	2.51 ± 0.06	1.032	4.688

TABLE 3.5: Observed final abundances[26][19][22], and the predictions by various BBN codes[23][21][29].

span of the values obtained by other codes.

Y_p

PRIMAT and PARTHENOPE both have very precise estimates for Y_p , which are mutually consistent. This is due to them both calculating the exact $p \rightleftharpoons n$ rates with very high precision. I get a slightly higher estimate, which is primarily due to the lack of incomplete neutrino decoupling, and that unlike PRIMAT and PARTHENOPE, the $n \rightleftharpoons p$ rate I use doesn't include bremsstrahlung corrections[13]. The effect of these corrections are given in Pitrou et al. [21, table V], as $\delta Y_p = 1.2 \times 10^{-4}$ and $\delta Y_p = -3.1 \times 10^{-4}$. If we correct for this, we get a final abundance of $Y_p \times 10 = 2.4721 + 0.0012 - 0.0031 = 2.4702$, which is consistent with both PRIMAT and PARTHENOPE.

^2H

Deuterium stands out with my implementation being outside the quoted uncertainty of both ALTERBBN and PRIMAT. As always, this is most likely due to a different choice of reaction rates. In particular, the rate for $^2\text{H} + n \rightarrow ^3\text{He}$, for which REACLIB uses a theoretical rate from Descouvemont et al. [12], as opposed to the other codes which use more recent experimental rates. For ALTERBBN and the 2018 snapshot of PRIMAT, this results in lower deuterium abundances. Yet it matches PARTHENOPE since they use a recent rate from LUNA, which is actually closer to the old theoretical rate than previous experimental rates[27].

^3He

For ^3He , my results match those of ALTERBBN and PARTHENOPE, with PRIMAT being slightly higher. Different reaction rates might explain this difference, but due to the poor observational constraints, this is not a major issue.

^7Li

^7Li is where we see the largest deviation. Relative to ALTERBBN, we know this is due to different reaction rates, and this is also the most probable explanation for PRIMAT. PARTHENOPE once again shows better agreement since they, in this case, use many of the same reaction rates as those in REACLIB. There is still a small difference,

which is likely to be caused by the lack of incomplete decoupling. Yet compared to the difference caused by different rates in PRIMAT and ALTERBBN, this is completely inconsequential, which once again justifies the omission of incomplete decoupling. Yet, every single code is still nowhere near the observational value, which is, of course, the infamous cosmological lithium problem.

3.3.1 η and the Lithium Problem

The most well-known illustration of the lithium problem is obtained by plotting the final abundances as a function of the primary free parameter of BBN η . At any specific time, the balance of various reaction rates is determined by the ratio of baryon density and temperature. Barring radically different physics, any cosmological solution to the lithium problem will involve modifying this ratio, for which η is a direct proxy. Since the REACLIB rates don't include the associated uncertainties, I am unable to make a direct estimate of the uncertainty of my results. However, since these uncertainties stem from the same reactions as those in other codes, I can use an average of these to get a reasonable upper bound on the uncertainty. Additionally, the predicted uncertainties of other codes are demonstrably too conservative. For figure 3.15, the estimated uncertainties used are $Y_p = 0.1\%$, $^2\text{H}=2\%$, $^3\text{He}=2\%$, and $^7\text{Li}=8\%$.

We see how my results match the expected abundances for all observable nuclei except lithium. We also see how any cosmological solution to this problem would inevitably lead to an even worse "deuterium problem".

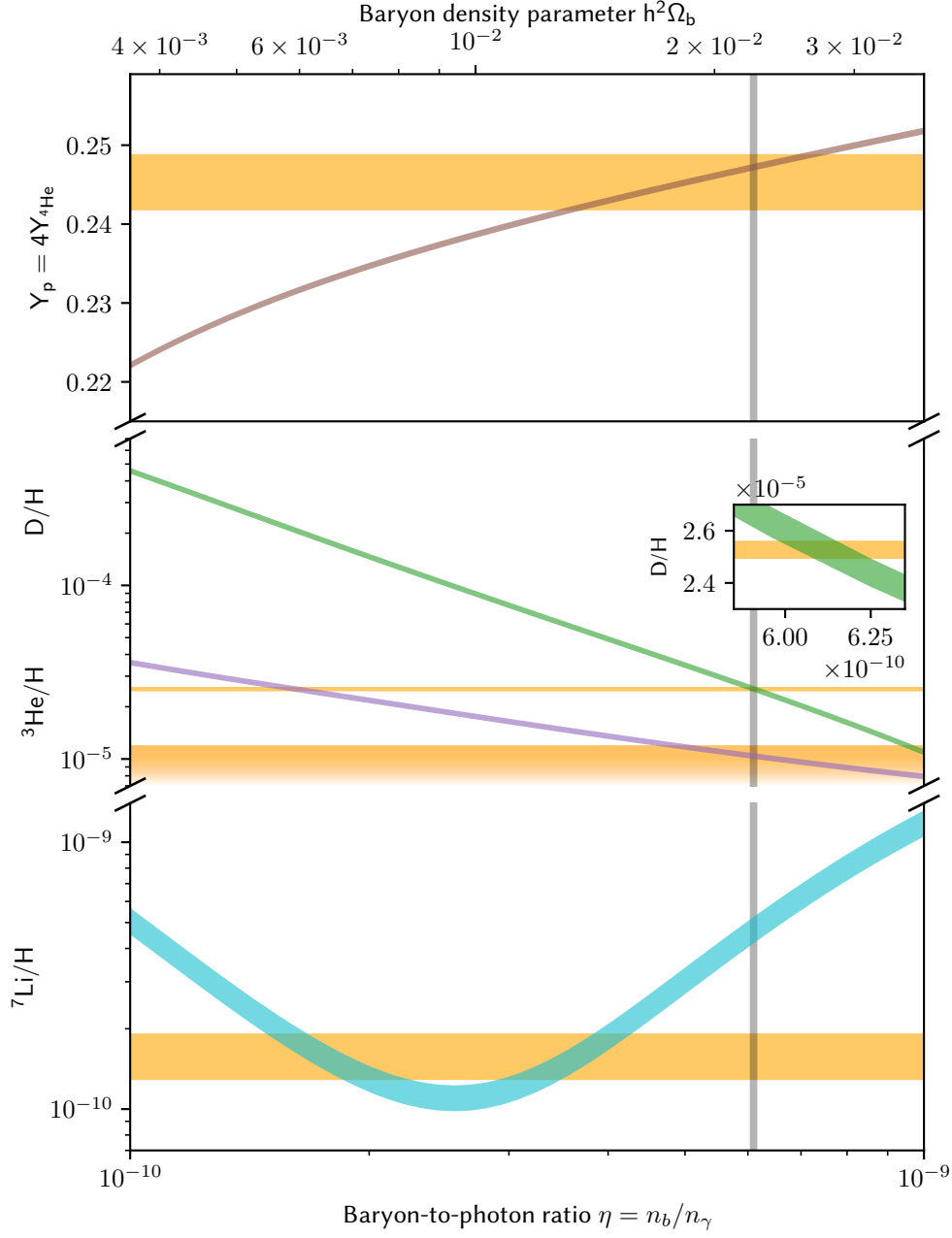


FIGURE 3.15: Resulting final abundances for different values of η . Gray lines represent the value for η from the most recent Planck results[24]. Orange represents the observational constraints given in table 3.5. The remaining lines are the abundances produced by APODORA, with uncertainties estimated based on those of comparable networks.

3.4 Outlook

The flexibility of APODORA will allow for easier investigations into the physical processes of BBN, especially nuclear processes.

One such use would be to systematically identify the relevant reactions for BBN. With the pynucastro interface, we can easily evaluate the different reaction rates without having to modify the actual BBN calculations. I previously used this to create the plots in appendix A and identify the primary rates mentioned at the beginning of chapter 3. This could be extended to create a new reaction network without the countless rates that don't significantly impact final abundances, which would be very useful, as the number of reaction rates that must be evaluated is one of the main factors increasing runtime. More importantly, systematically identifying these rates would be useful not only to this but to every single BBN code.

To further improve speed at the cost of accessibility, the solution methods in APODORA could be implemented in a compiled language such as C and C++. This has the potential to be one of, if not the fastest BBN code currently available. Most of the required calculations are quite simple and would be easy to implement, with the main exceptions being the modified Bessel functions and the Radau IIA integration method. These, however, are well known and have many existing implementations[10]. For the reaction network, pynucastro supports generating the network in both Python and C++.

A C/C++ version of APODORA would also be very useful for interfacing directly with CLASS[16]. The Cosmic Linear Anisotropy Solving System is a Boltzmann code that calculates the theoretical power spectrum based on cosmological parameters. The ability to also make predictions on BBN abundances would be an excellent way to provide additional constraints when testing cosmological models. Among the various available Boltzmann codes, CLASS is an obvious choice, as its stated goals of user-friendliness, flexibility, accuracy, and speed[16], are the same as those of this BBN code. But of course, the primary reason for integrating APODORA with CLASS is that my supervisor is one of the main developers.

Another use would be to compare the background calculation of various BBN non-BBN codes, as was done with ALTERBBN in section 3.2.3. This is only possible due to APODORA completely separating the calculation of background parameters and nuclear processes. The modular structure could even lead to multiple unique codes for calculating either the background or the reaction network. This would make it much easier to compare BBN codes, as it would definitively identify what or if differences are cosmological or nuclear in origin.

Conclusion

We derived every equation necessary for the computation of background parameters with sufficient precision. This includes an updated version of the classic derivation of e^-e^+ density and pressure originally performed by Chandrasekhar [1], and a correction to the initial time as presented by Wagoner[4], as well as the incomplete correction by Sharpe[28].

A BBN code was created to fulfill the five requirements stated in the introduction.

- **Accessibility:** APODORA requires nothing except Python and publicly available packages. It is currently available on my personal GitHub page <https://github.com/hansbdein> with a clean and properly documented version being released in the near future at <https://github.com/AarhusCosmology>.
- **Accuracy:** APODORA was demonstrated to have numerical precision equal to or superior to that of contemporary codes. The accuracy of Y_p is slightly lower than that of PRIMAT and PARTHENON due to the lack of incomplete neutrino decoupling and a direct calculation of the $p \rightleftharpoons n$ rate. This is acceptable since the accuracy is still well within the observational constraints and that of other codes without an explicit focus on accurate Y_p predictions.
- **Alacrity:** Using optimal precision parameters, APODORA is just as fast as other BBN codes with an average runtime of 0.61 seconds on an Intel i3-1115G4 @ 3.00GHz.
- **Agnostic reaction rates:** A reaction network was created using rates from the REACLIB database[15], eliminating any need for manual rate selection.
- **Adaptability:** APODORA was implemented in a modular fashion, with the reaction network and calculation of cosmological parameters being independent of the main integration routine. The main routine is in a Jupyter Notebook, allowing for easy access to every parameter at all times during the process of BBN.

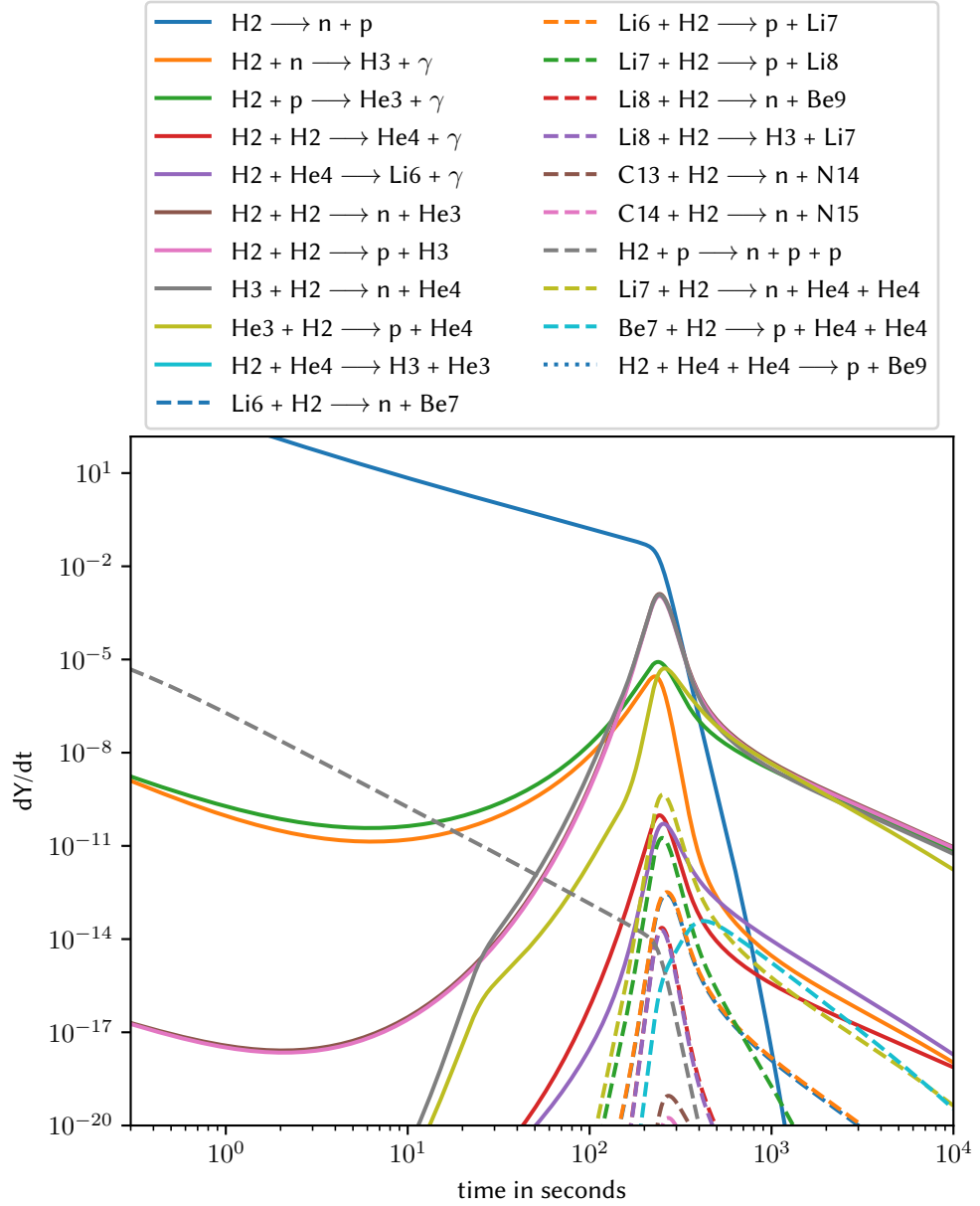
Bibliography

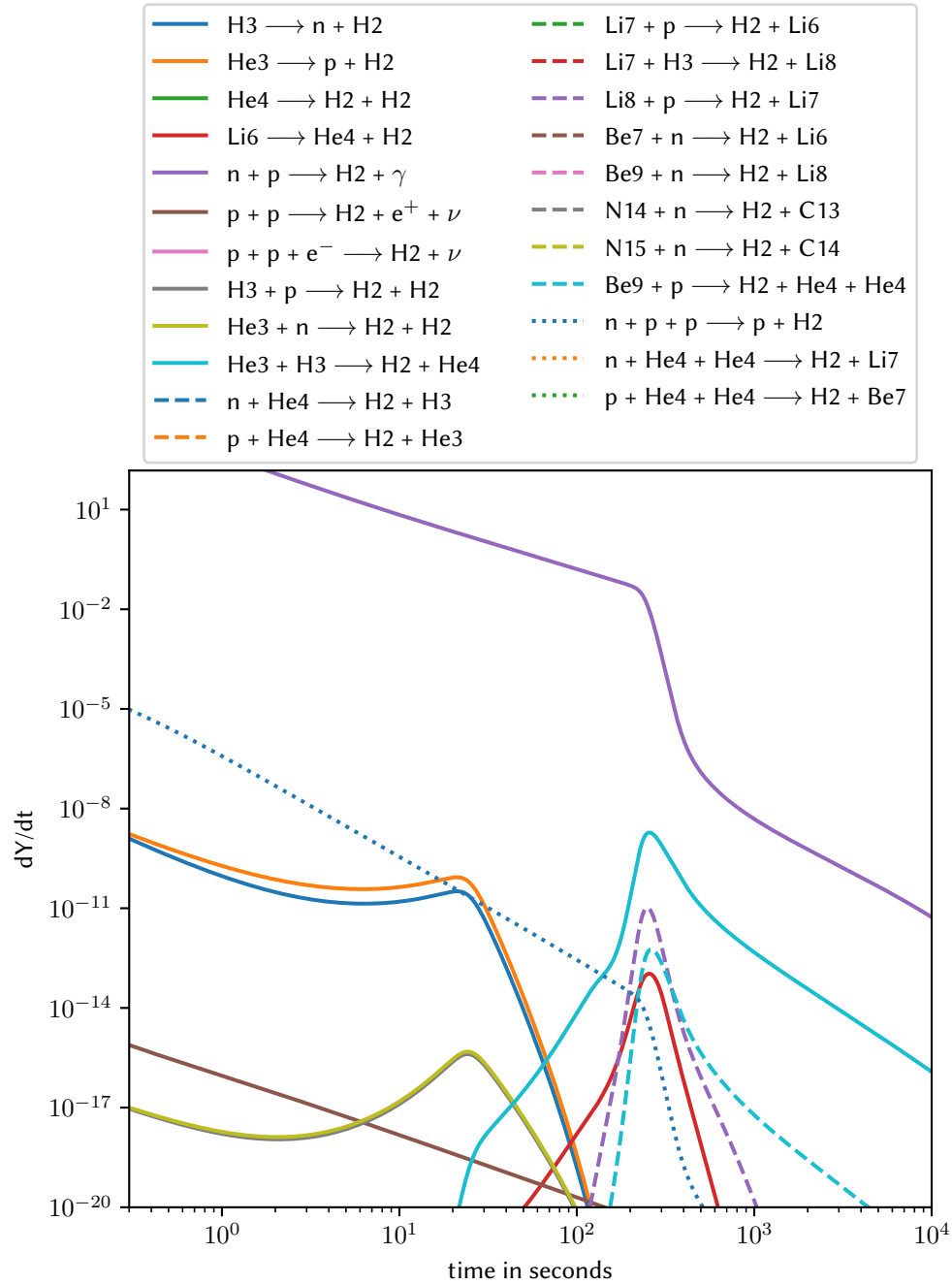
- [1] S. Chandrasekhar. *An Introduction to the Study of Stellar Structure*. First Edition. THE UNIVERSITY OF CHICAGO PRESS, 1939.
- [2] R. A. Alpher, H. Bethe, and G. Gamow. “The Origin of Chemical Elements”. In: *Phys. Rev.* 73 (7 Apr. 1948), pp. 803–804.
- [3] P. J. E. Peebles. “Primordial Helium Abundance and the Primordial Fireball. II”. In: *The Astrophysical Journal* 146 (Nov. 1966), p. 542.
- [4] Robert V. Wagoner, William A. Fowler, and F. Hoyle. “On the Synthesis of Elements at Very High Temperatures”. In: *The Astrophysical Journal* 148 (Apr. 1967), p. 3.
- [5] Robert V. Wagoner. “Synthesis of the Elements Within Objects Exploding from Very High Temperatures”. In: *The Astrophysical Journal Supplement* 18 (June 1969), p. 247.
- [6] Robert Wagoner. “Big-Bang Nucleosynthesis Revisited”. In: *The Astrophysical Journal* 179 (Dec. 1972), pp. 343–360.
- [7] Lawrence Kawano. “Let’s go: Early universe. 2. Primordial nucleosynthesis: The Computer way”. In: (Jan. 1992).
- [8] E. Kolb and M. Turner. *The Early Universe*. Frontiers in physics. Avalon Publishing, 1994.
- [9] Steen Hannestad and Jes Madsen. “Neutrino decoupling in the early universe”. In: *Phys. Rev. D* 52 (1995), pp. 1764–1769.
- [10] M.G.R. Vogelaar. *bessel.c*. <https://www.atnf.csiro.au/computing/software/gipsy/sub/bessel.c>. 1998.
- [11] B. Ryden. *Introduction to cosmology*. Second Edition. Cambridge University Press, 2002.
- [12] Pierre Descouvemont, Abderrahim Adahchour, Carmen Angulo, Alain Coc, and Elisabeth Vangioni-Flam. “Compilation and R-matrix analysis of Big Bang nuclear reaction rates”. In: *Atomic Data and Nuclear Data Tables* 88.1 (Sept. 2004), pp. 203–236.
- [13] P D Serpico et al. “Nuclear reaction network for primordial nucleosynthesis: a detailed analysis of rates, uncertainties and light nuclei yields”. In: *Journal of Cosmology and Astroparticle Physics* 2004.12 (Dec. 2004), pp. 010–010.

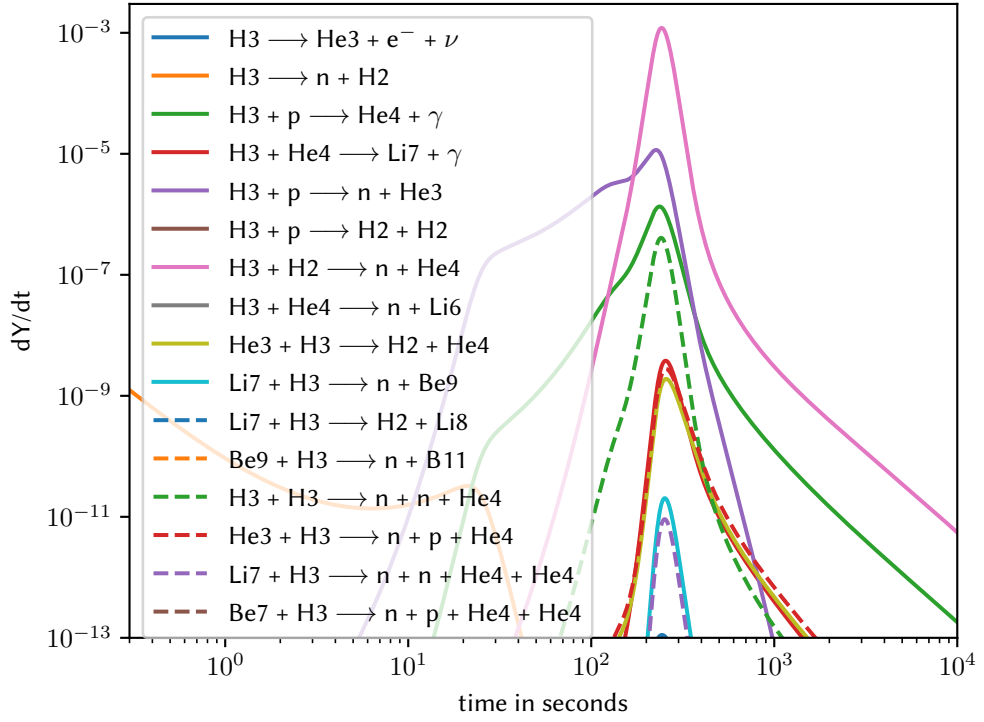
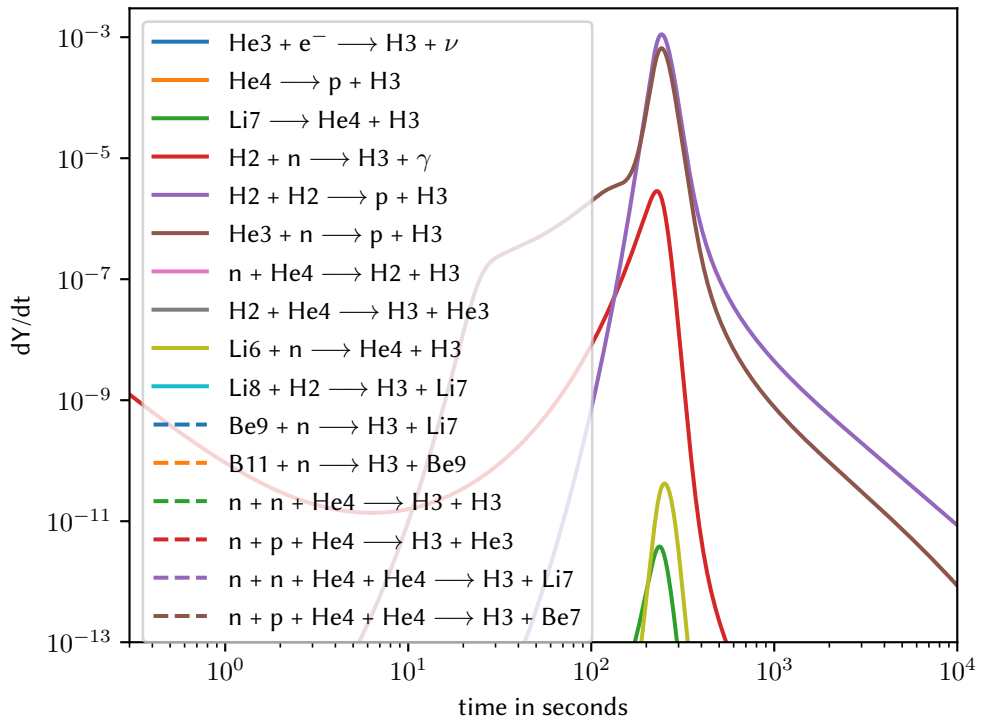
- [14] Fernando Pérez and Brian E. Granger. “IPython: a System for Interactive Scientific Computing”. In: *Computing in Science and Engineering* 9.3 (May 2007), pp. 21–29.
- [15] Richard H. Cyburt et al. “The JINA REACLIB Database: Its Recent Updates and Impact on Type-I X-ray Bursts”. In: *The Astrophysical Journal Supplement* 189.1 (July 2010), pp. 240–252.
- [16] Diego Blas, Julien Lesgourgues, and Thomas Tram. “The Cosmic Linear Anisotropy Solving System (CLASS). Part II: Approximation schemes”. In: *Journal of Cosmology and Astroparticle Physics* 2011.07 (July 2011), pp. 034–034.
- [17] Alain Coc et al. “New reaction rates for improved primordial D/H calculation and the cosmic evolution of deuterium”. In: *Phys. Rev. D* 92 (12 Dec. 2015), p. 123526.
- [18] Pablo F. de Salas and Sergio Pastor. “Relic neutrino decoupling with flavour oscillations revisited”. In: *Journal of Cosmology and Astroparticle Physics* 2016.07 (July 2016), pp. 051–051.
- [19] Ryan J. Cooke, Max Pettini, and Charles C. Steidel. “One Percent Determination of the Primordial Deuterium Abundance*”. In: *The Astrophysical Journal* 855.2 (Mar. 2018), p. 102.
- [20] David J. Griffiths and Darrell F. Schroeter. *Introduction to quantum mechanics*. Third edition. Cambridge ; New York, NY: Cambridge University Press, 2018.
- [21] Cyril Pitrou, Alain Coc, Jean-Philippe Uzan, and Elisabeth Vangioni. “Precision big bang nucleosynthesis with improved Helium-4 predictions”. In: *Submitted to Phys. Rept.* (2018).
- [22] M. Tanabashi et al. “Review of Particle Physics”. In: *Phys. Rev. D* 98 (3 Aug. 2018), p. 030001.
- [23] A. Arbey, J. Auffinger, K. P. Hickerson, and E. S. Jenssen. *AlterBBN v2: A public code for calculating Big-Bang nucleosynthesis constraints in alternative cosmologies*. 2019.
- [24] Planck Collaboration et al. “Planck 2018 results. VI. Cosmological parameters”. In: *Astronomy and Astrophysics* 641, A6 (Sept. 2020), A6.
- [25] Pauli Virtanen et al. “SciPy 1.0: Fundamental Algorithms for Scientific Computing in Python”. In: *Nature Methods* 17 (2020), pp. 261–272.
- [26] Erik Aver et al. “Improving helium abundance determinations with Leo P as a case study”. In: *Journal of Cosmology and Astroparticle Physics* 2021.03 (Mar. 2021), p. 027.
- [27] O. Pisanti, G. Mangano, G. Miele, and P. Mazzella. “Primordial Deuterium after LUNA: concordances and error budget”. In: *Journal of Cosmology and Astroparticle Physics* 2021.04 (Apr. 2021), p. 020.
- [28] Charlie Sharpe, Geraint F. Lewis, and Luke A. Barnes. *Big Bang Nucleosynthesis Initial Conditions: Revisiting Wagoner et al. (1967)*. 2021.

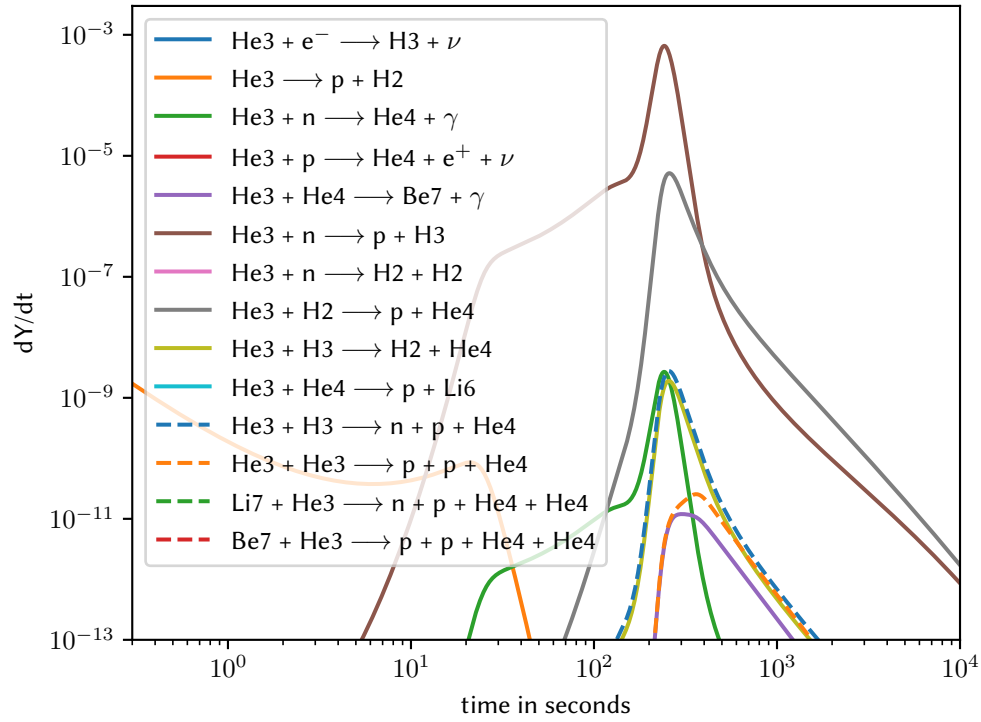
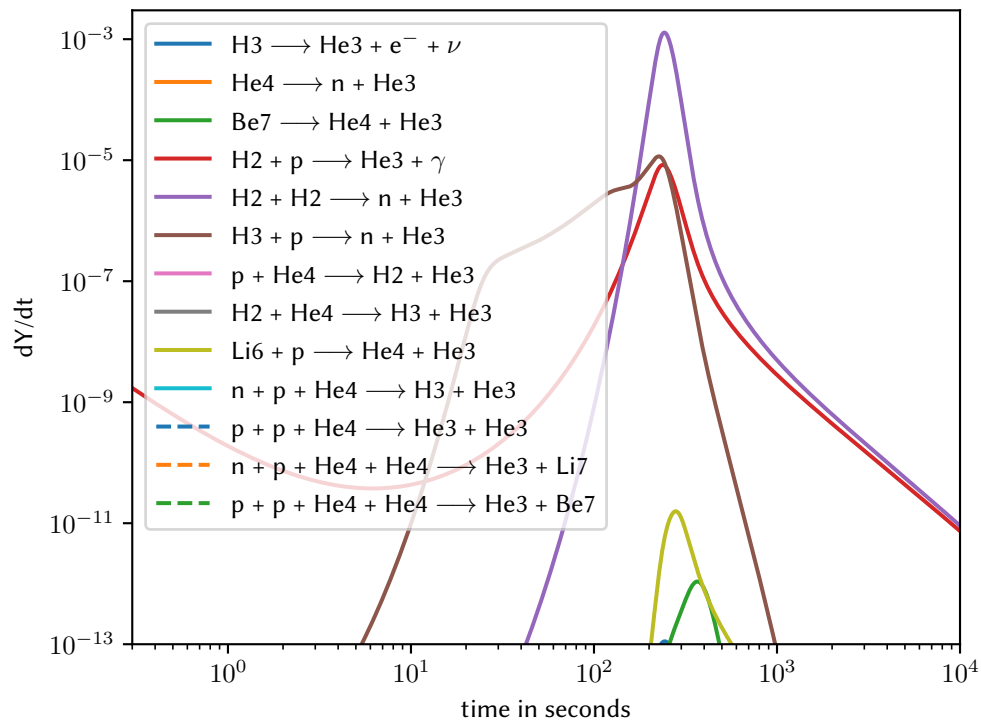
- [29] S. Gariazzo, P. F. de Salas, O. Pisanti, and R. Consiglio. “ParthENoPE revolutions”. In: *Computer Physics Communications* 271 (Feb. 2022), p. 108205.
- [30] Ralf S. Klessen and Simon C. O. Glover. *The first stars: formation, properties, and impact*. 2023.
- [31] Alexander I. Smith et al. “pynucastro: A Python Library for Nuclear Astrophysics”. In: *The Astrophysical Journal* 947.2 (Apr. 2023), p. 65.
- [32] *Cosmic History*. <https://science.nasa.gov/universe/overview/>. NASA.
- [33] *NIST Digital Library of Mathematical Functions*. <https://dlmf.nist.gov/>, Release 1.1.11 of 2023-09-15. F. W. J. Olver, A. B. Olde Daalhuis, D. W. Lozier, B. I. Schneider, R. F. Boisvert, C. W. Clark, B. R. Miller, B. V. Saunders, H. S. Cohl, and M. A. McClain, eds.

Plots of Reaction rates during BBN

FIGURE A.1: Strength of the different 2H destruction rates, at different times during BBN.

FIGURE A.2: Strength of the different ^2H creation rates, at different times during BBN.

FIGURE A.3: Strength of the different ${}^3\text{H}$ destruction rates, at different times during BBN.FIGURE A.4: Strength of the different ${}^3\text{H}$ creation rates, at different times during BBN.

FIGURE A.5: Strength of the different ${}^3\text{He}$ destruction rates, at different times during BBN.FIGURE A.6: Strength of the different ${}^3\text{He}$ creation rates, at different times during BBN.

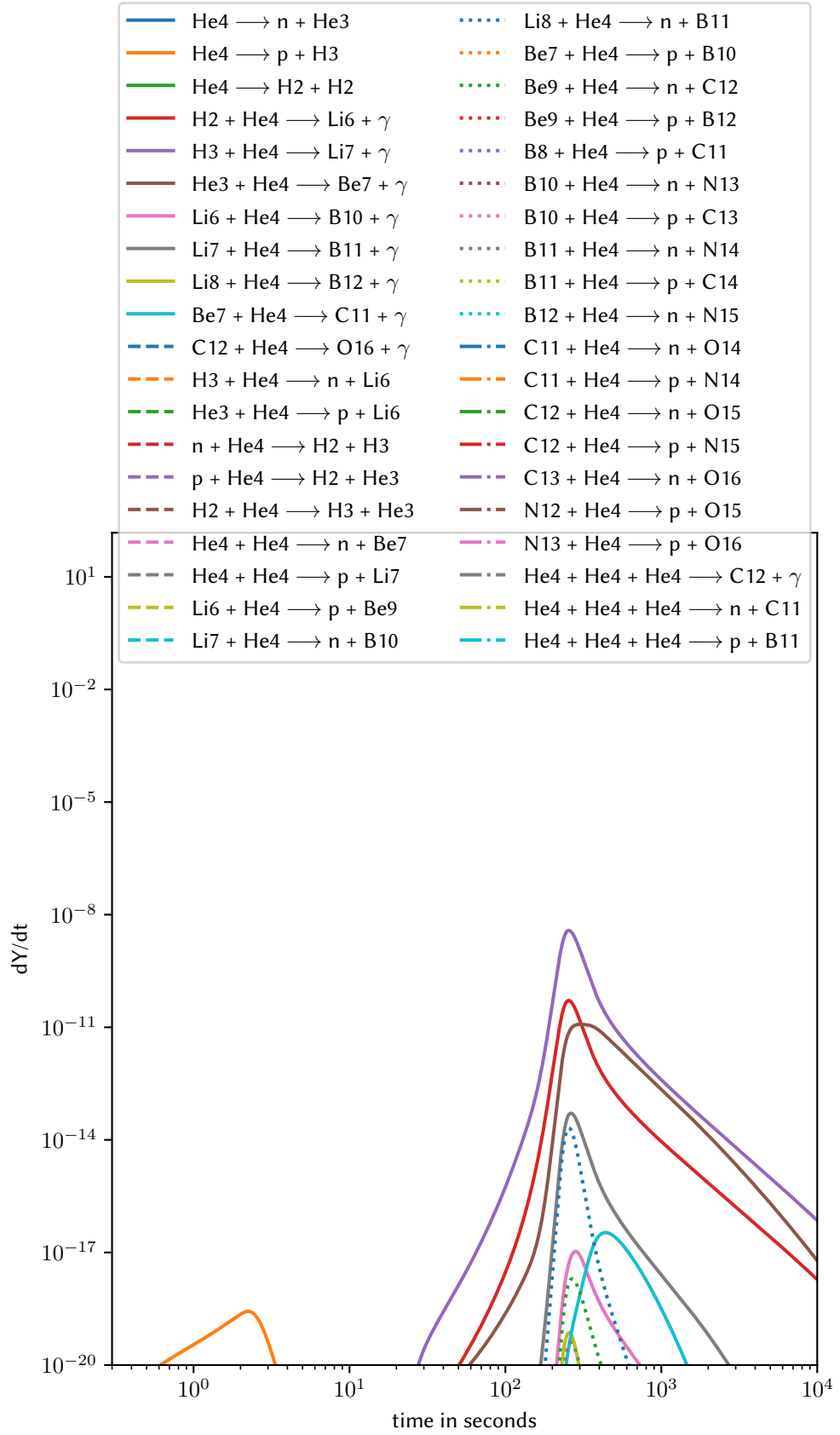


FIGURE A.7: Strength of the different ${}^4\text{He}$ destruction rates, at different times during BBN, Excluding all 3 and 4 body reactions except triple-alpha.

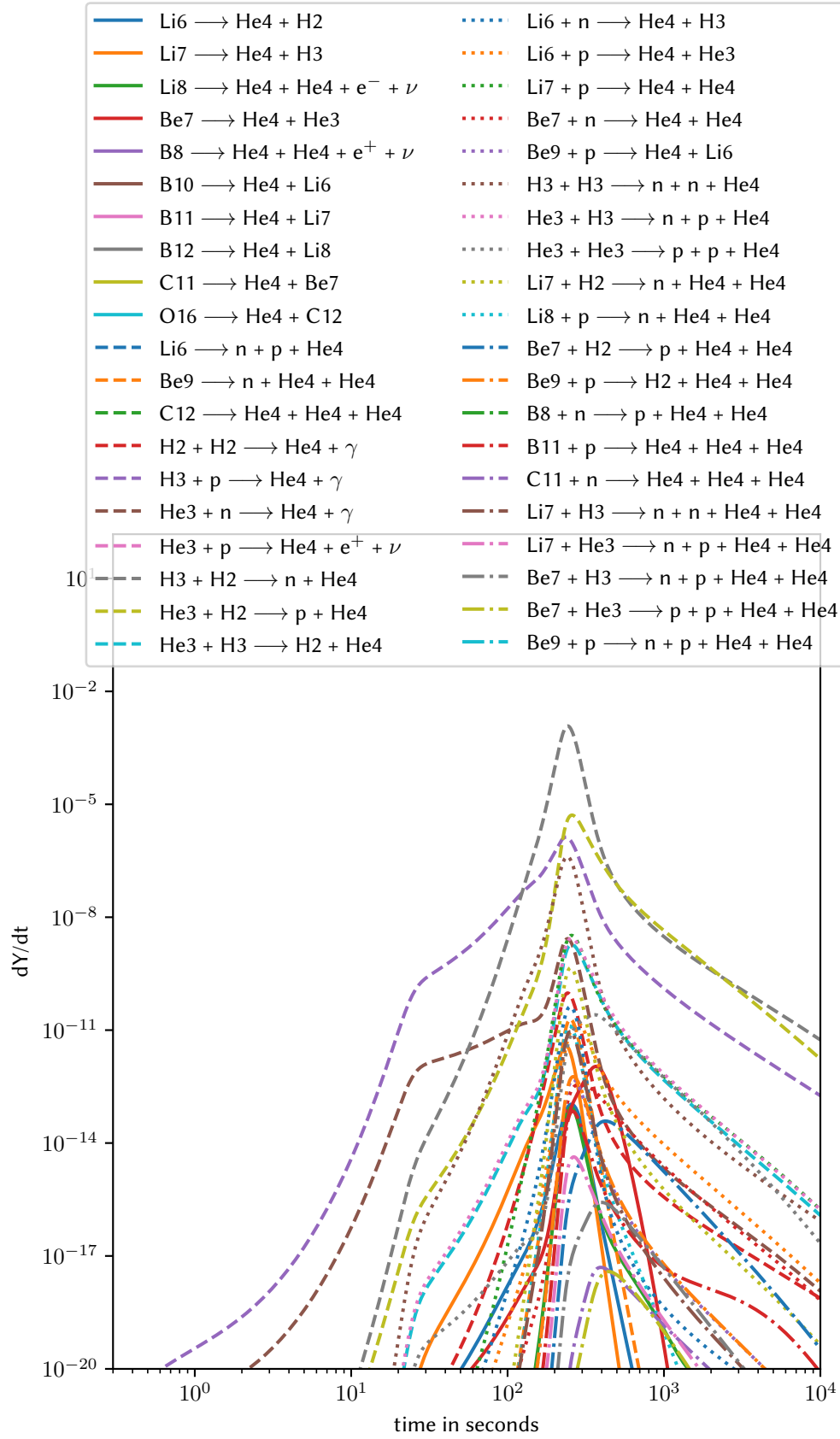
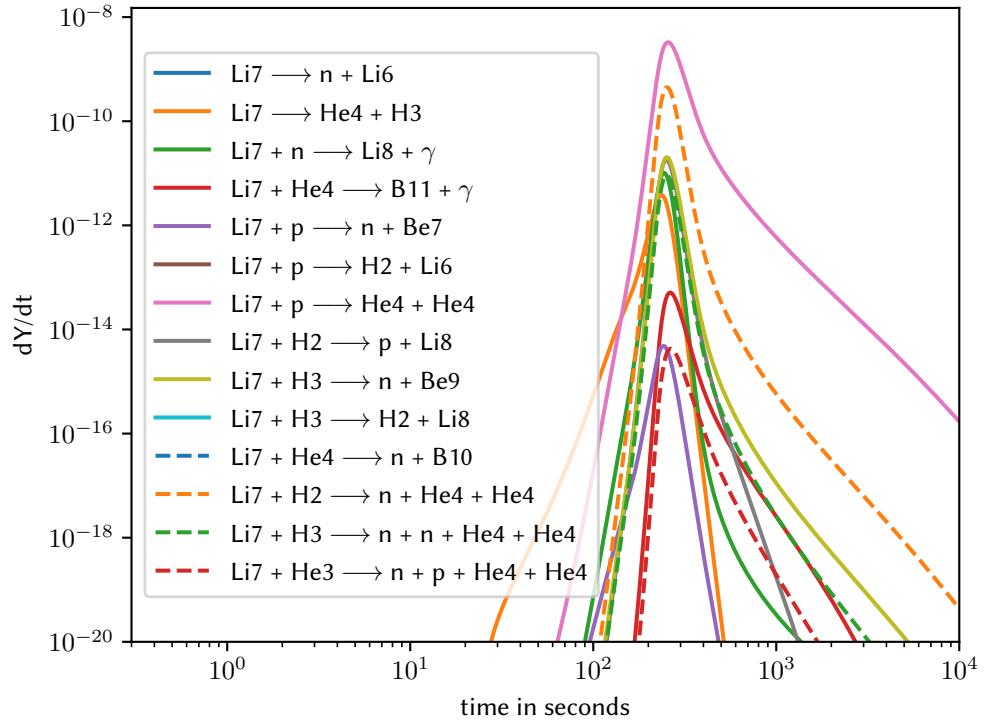
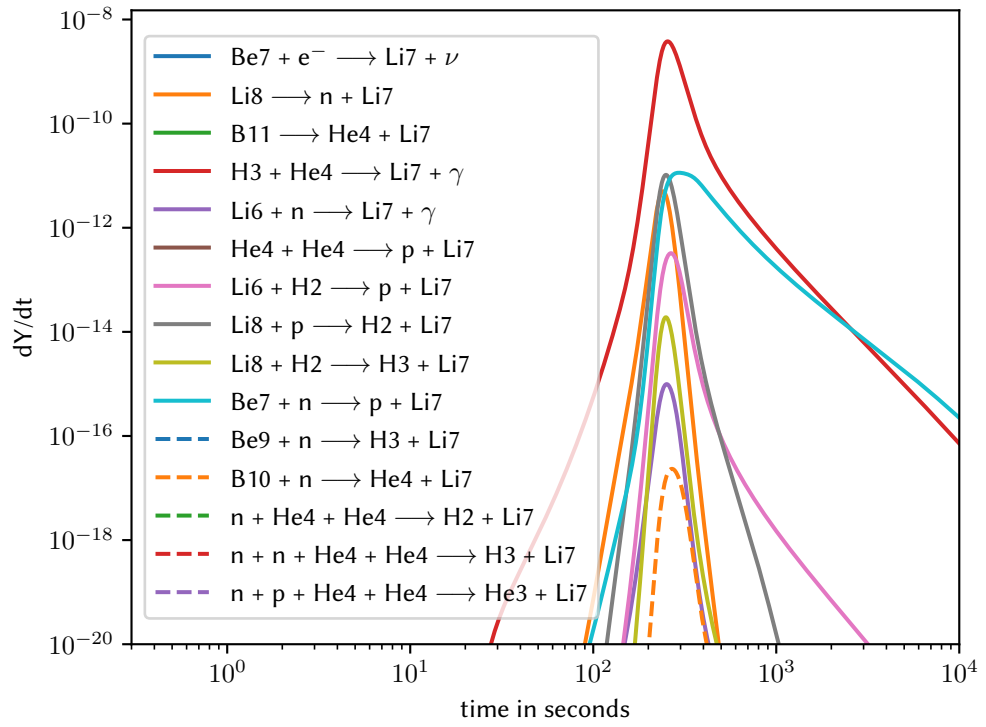
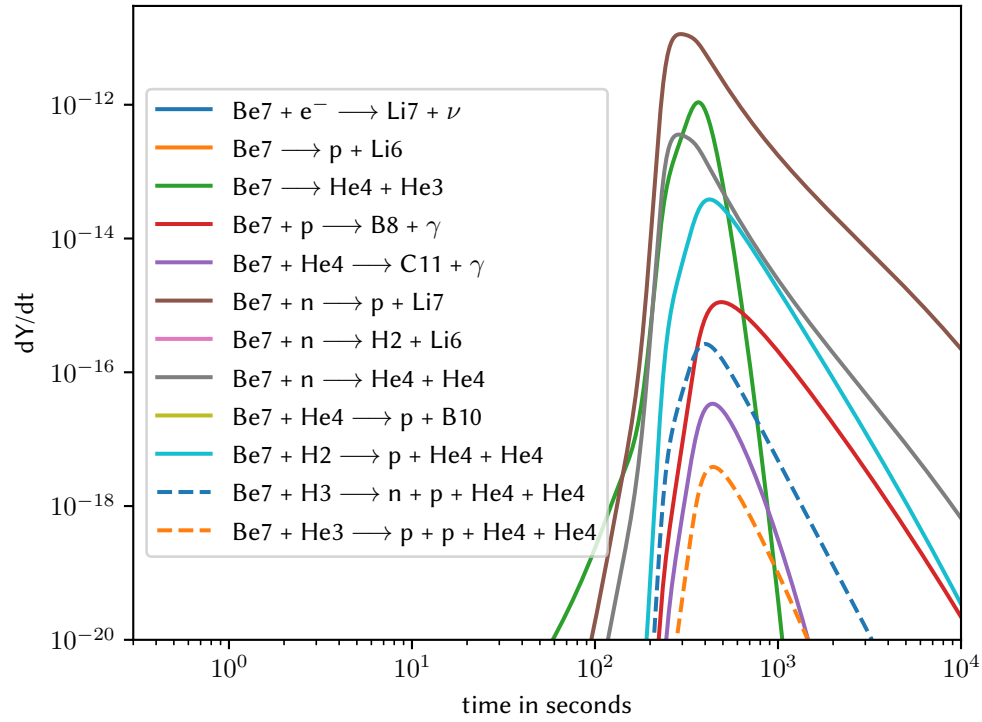
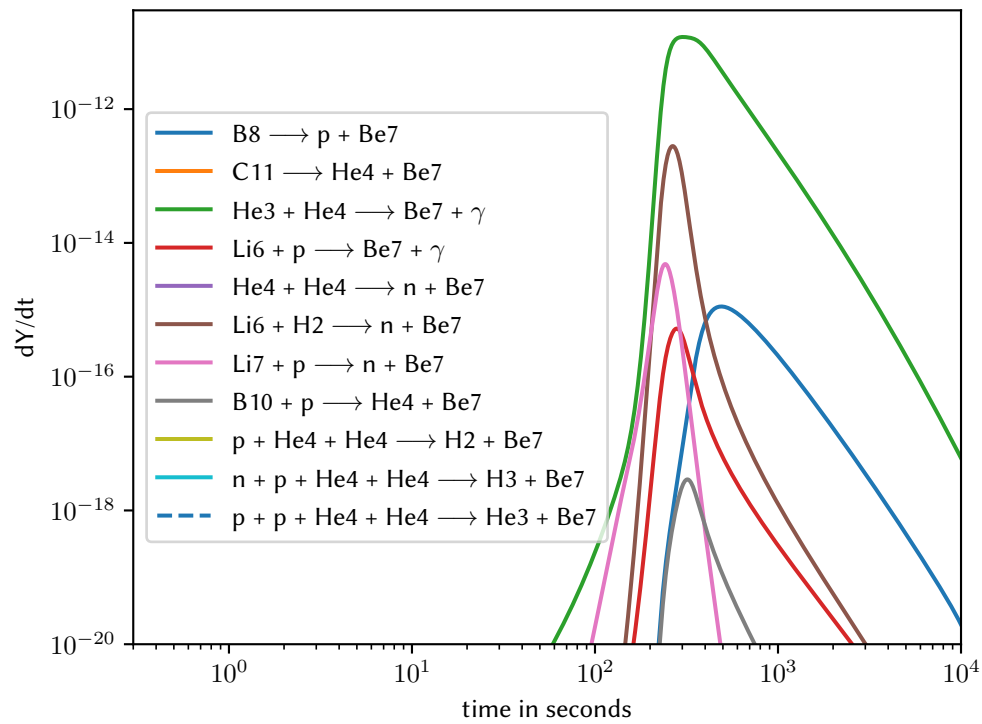


FIGURE A.8: Strength of the different ^4He creation rates, at different times during BBN, excluding rates due to proton and neutron capture on heavy nuclei with $A > 9$.

FIGURE A.9: Strength of the different ${}^7\text{Li}$ destruction rates, at different times during BBN.FIGURE A.10: Strength of the different ${}^7\text{Li}$ creation rates, at different times during BBN.

FIGURE A.11: Strength of the different ${}^7\text{Be}$ destruction rates, at different times during BBN.FIGURE A.12: Strength of the different ${}^7\text{Be}$ creation rates, at different times during BBN.